Modelling of barotropic M_2 tidal circulation with friction effects in Kyuquot Sound

by

Di Wan
B.Sc., University of Calgary, 2007

A Dissertation Submitted in Partial Fulfillment of the
Requirements for the Degree of

Master of Science

in the Department of Physics and Astronomy

© Di Wan, 2013
University of Victoria

All rights reserved. This dissertation may not be reproduced in whole or in part, by photocopying or other means, without the permission of the author.

Modelling of barotropic M_2 tidal circulation with friction effects in Kyuquot Sound

by

Di Wan
B.Sc., University of Calgary, 2007

Supervisory Committee

Dr. Jody Klymak, Co-Supervisor
(Department of Physics and Astronomy)

Dr. Mike Foreman, Co-Supervisor
(Institute of Ocean Sciences)

Dr. Steve Cross, Committee Member
(Department of Geography)

Supervisory Committee

Dr. Jody Klymak, Co-Supervisor
(Department of Physics and Astronomy)

Dr. Mike Foreman, Co-Supervisor
(Institute of Ocean Sciences)

Dr. Steve Cross, Committee Member
(Department of Geography)

ABSTRACT

This thesis examines the barotropic M_2 tidal circulation and associated oceanographic properties in the Kyuquot Sound. The main contribution of this thesis is the development of a simple analytical model based on results from a Finite-Volume Coastal Ocean Model (FVCOM), describing a two-channel system. The simple analytical model allows us to estimate the energy dissipation rate in Crowther Channel and recognizes that friction is responsible for phase difference (between currents and elevation) variations as we move along the channel. This is done without running complex numerical models or collecting extensive observation data. We find a difference in velocity phases between a dominant channel (Kyuquot Channel) and a secondary channel (Crowther Channel) in Kyuquot Sound. The velocity phase response in the secondary channel is out of phase with the dominant channel, and varies when we move along the channel, while the elevation phases are consistent between the two channels. This result has a potentially significant impact on future biological and navigation decisions. Our research is also focused on getting a general understanding of the circulation in Kyuquot Sound, and offers an energy budget comparison between the analytical and numerical model results. These results allow the contrast between the simple analytical and the numerical model to be clarified, as the advantages and limitations of both are discussed in detail.

Contents

List of Tables

List of Figures

ACKNOWLEDGEMENTS

I would like to thank:

my co-supervisors, Dr. Mike Foreman and Dr. Jody Klymak: Mike, for constantly encouraging me to follow my own ideas, and patiently guiding me through the details; Jody, for teaching me to think as an Ocean Physicist;

my committee member, Dr. Steve Cross, for having me in the CIMTAN project and introducing me to a much bigger world beyond Physics;

my family, friends, other graduate students and colleagues at IOS, for all their support, friendship, and inspiration.

A special thank you goes to the Canadian Integrated Multi-Tropic Aquaculture Network (CIMTAN). This work would not have been possible without the funding from CIMTAN and all the inspiration from everyone that I met through the network.

Chapter 1

Introduction

This thesis examines the barotropic M_2 tidal circulation and associated oceanographic properties in the Kyuquot Sound. The main contribution of this thesis is the development of a simple analytical model based on results from a Finite-Volume Coastal Ocean Model (FVCOM), describing a two-channel system. The simple analytical model allows us to estimate the energy dissipation rate in Crowther Channel and recognize that friction is responsible for phase difference (between currents and elevation) variations as we move along the channel without running complex numerical models or collecting extensive observation data. We find a difference in velocity phases between a dominant channel (Kyuquot Channel) and a secondary channel (Crowther Channel) in Kyuquot Sound. The velocity phase response in the secondary channel is out of phase with the dominant channel, and varies when we move along the channel, while the elevation phases are consistent between the two channels. This result has a potentially significant impact on future biological and navigation decisions. Our research is also focused on getting a general understanding of the circulation in Kyuquot Sound, and offers an energy budget comparison between the analytical model results and numerical model results. These results allow the contrast between the simple analytical and the numerical model to be clarified, as the advantages and limitations of both are discussed in detail.

Kyuquot Sound (Fig. 1.1), located on the northwestern coast of Vancouver Island, is an important aquaculture location. It represents an area where natural populations of sable fish reside as part of their coastal-offshore life cycle. Therefore, investigations of oceanographic conditions in the sound are relevant to existing and future aquaculture sites. Some previous modeling work has included this region. Masson and Fine (2012) implemented a large scale model on the west coast British Columbia using

the Regional Ocean Modelling System (ROMS) with a 3 km horizontal resolution, encompassing Kyuquot Sound. This work is important at offering a general idea of the offshore circulation conditions of the west coast Vancouver Island, but it did not study the circulation in Kyuquot Sound in detail. They demonstrated that the seasonal variability of the coastal circulation had contributions from both remote (at outer boundaries) and local (direct wind stress over the domain) forcing. A finer resolution model is needed to provide sufficient information for developing more efficient aquaculture production systems.

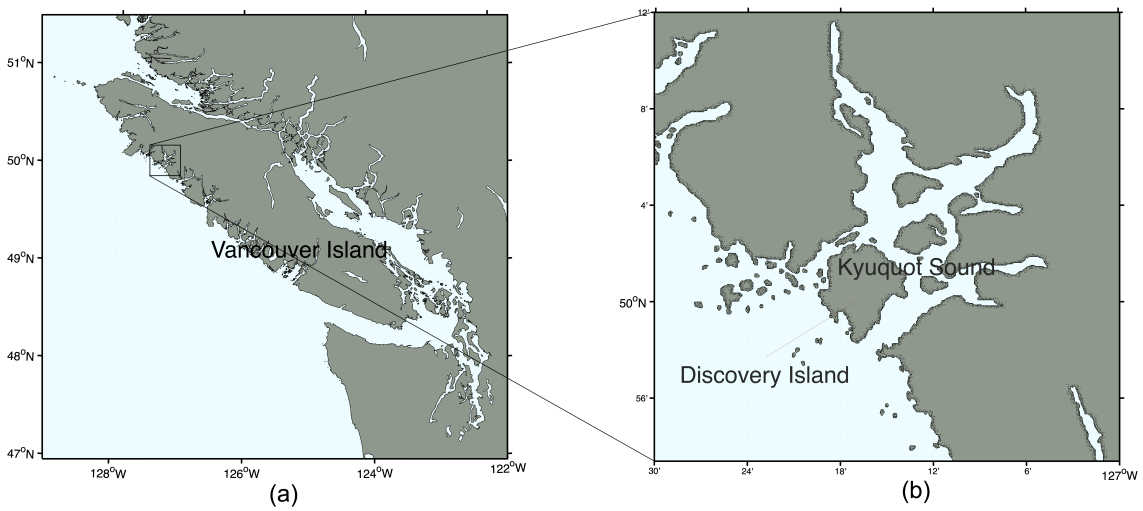

Figure 1.1: (a) Vancouver Island. (b) Kyuquot Sound.

The biological significance of Kyuquot Sound makes understanding flow patterns in this region very interesting and important. In particular, an integrated multi-trophic aquaculture (IMTA) site - KyuquotSeafoods (see Fig. 1.2), which is located in Discovery Channel, will benefit from further understanding of the circulation in terms of improving the system's environmental remediation and economic stability. IMTA combines fed aquaculture with inorganic extractives (such as kelp, which extract inorganic nutrients) and organic extractives (such as shellfish, which extract organic nutrients) to potentially produce a more environmentally friendly system. By-products from IMTA, including wastes, from one species are used as food and/or fertilizer inputs for another. Fin-fish is the primary species in aquaculture. Being at the top tropic level, they release organic nutrients as well as inorganic tracers such as ammonia. These excessive nutrients and uneaten feed associated with fish farms need to be extracted as much as possible by other species at lower trophic levels in

IMTA systems. By changing the orientation of fish cages and relative positions of all species, it is possible to increase the amount of biomass extraction and limit the input of excessive nutrients to the open ocean.

Aside from ecological motivations, investigating current circulation will also benefit navigation. Tide and current tables are key navigational aids for captains and fishermen. Current predictions are only available at limited stations, so navigation is largely dependent on estimations based on available information at major stations. If two channels are close to one another, and the only available current information is for the primary channel, it might be assumed that the currents of the secondary channel will behave similarly. Often times, this is the case when non-tidal flows are largely affected by topography, wind stress, fresh water runoffs, and other direct but local forcings (Beach and Stacey, 2005). But as will be seen, it is not the case here.

Tidal circulation dynamics and responses in fjord-like inlets have been extensively studied since early 1900. In classical estuary hydrodynamics, tidal currents are most easily understood as standing waves, especially in deep fjords. Research conducted in Quatsino Sound [**?**], Nootka Sound [**?**], Alberni Inlet [**?**] recognized that tidal forcing along with freshwater runoffs and winds, is one of the most significant contributions to currents in the fjords. More recently, **?** observed that the tidal currents in Knight Inlet were relatively uniform with depth. In deep fjords, the barotropic tide typically behaves like a nearly perfect standing wave (Klymak and Gregg, 2004). The tidal energy is reflected at the end of inlet (landward) nearly 100 % efficiency, if the energy lost to the bottom friction and internal motions is small compared to the total energy flux.

These classical hydrodynamics are not exactly true when friction is introduced. When friction is present in a channel, the phase difference between the currents and elevation can vary continuously along the channel (Sverdrup, 1942, p. 574). A large amount of effort has been made by researchers on further understanding the effects of friction on circulation in inlets. Hunt (1964) studied the tidal dynamics in the Thames River, disputing the classical terms ('standing waves' v.s. 'progressive waves') that were used to describe tidal flows. Most importantly, he pointed out friction is the cause of phase difference between currents and sea surface elevation along channels. An across-channel area integrated energy flux calculation was suggested by Garrett (1975). Using this method, Freeland and Farmer (1980) estimated the energy withdrawn by friction in Knight Inlet by measuring differences in elevation phases at two ends of a sill, and found that the major energy sink was in a straight

section containing the large sill. Other researchers [Stacey (1984, 1985); Klymak and Gregg (2004)] also studied Knight Inlet, mostly focusing on energy removal due to stratification and topography.

Topography plays an important role in the circulation in inlets. Klymak and Gregg (2004) investigated turbulence over the Knight Inlet sill, and found one-third of the barotropic total tidal energy was lost near the sill. Topographic effect forces a clockwise circulation around an intervening island in the middle of Puget Sound (Bretschneider et al., 1985) because the deep water coming from the East Passage (the east channel) gets mixed at the south of the basin and forms a seaward flow in Colvos Passage (the west channel). Similarly, circulation and mixing processes were examined in the St. Lawrence Estuary by **?**, showing that mixing was found near Ile-aux-Coudres, an island in the middle of the estuary.

These circulations in Puget Sound and St. Lawrence Estuary have not been studied systematically as a two-channel system. In Kyuquot Sound, an intervening island (Discovery Island, see Fig. 1.1) is in the middle of Kyuquot Sound, forming a two-channel system in the Sound. An along-channel phase difference between currents and elevation is observed in Crowther Channel of Kyuquot Sound, while based on results of a barotropic numerical model the adjacent channel (Kyuquot Channel) does not show such a feature. This result is peculiar and interesting. Recently developments of different numerical modelling methods have been providing the ability of predicting relatively accurate circulation patterns. However, it will still be valuable to have an analytic solution to the circulation of a two-channel system so we can have a conceptual understanding of the dynamics, and potentially apply it to other geographically similar two-channel systems.

The primary objective of this thesis is to find an analytic solution to the circulation in Kyuquot Sound that explains the along-channel varied phase difference between currents and elevations observed in the Crowther Channel. Stacey (1984, 1985); de Young and Pond (1987) and Klymak and Gregg (2004) found that internal waves due to stratification and topography are responsible for most of the energy loss in inlets when we have deep channels in different fjord-like regions. However when the channel is relatively shallow, friction is responsible for most of the energy dissipation. Tinis and Pond (2001) showed that the barotropic tidal energy flux in Sechelt Inlet is only a small amount (less than 0.5%) of the energy flux that was lost to bottom dissipation. In addition, for both the analytic solution and numerical modelling results we also compare the energy withdrawn by the frictional process that is directly

associated with the phase difference.

Conducting energy budget investigation in a numerical model is the secondary objective of this thesis. Energy balance is often used to provide stability measures for numerical models (Ferziger and Peric, 2002). An unstructured Finite-Volume Coastal Ocean Model (FVCOM) (Chen et al., 2003, 2006, 2011) is employed to examine the tidal and sub-tidal circulation and hydrodynamics in Kyuquot Sound. Recognizing the flow patterns and examining the energy budget from FVCOM results provide some credibility for the numerical model. A number of methods were proposed and implemented to calculate energy balance numerically, e.g., energy flux in Chesapeake Bay by Zhong and Li (2006) with Regional Ocean Modeling System (ROMS), and M_2 barotropic-to-baroclinic energy conversion in Hawaiian Islands by Carter et al. (2008) using Princeton Ocean Model (POM). The energy budget calculation method in this thesis loosely follows the method established by Carter et al. (2008).

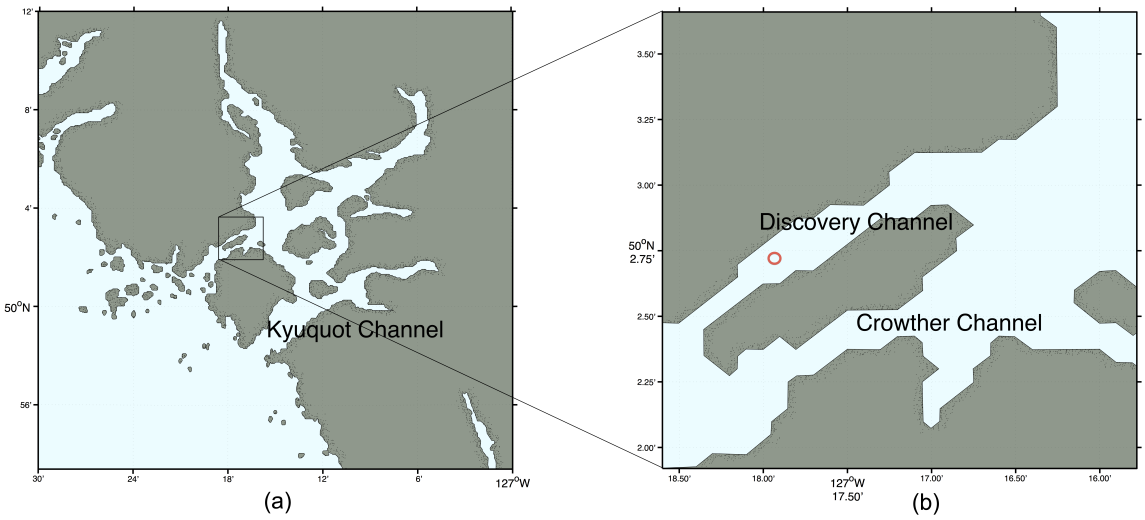

Figure 1.2: Left: Kyuquot Sound. Right: KyuquotSeafood Farm.

This rest of this thesis is organized as follows:

Chapter 2 provides an overview of FVCOM model setup and different forcing fields that are applied to the model.

Chapter 3 presents some results from the model base run, and is focused on the velocity phase differences between two channels in Kyuquot Sound.

Chapter 4 describes an analytical two-channel system model for Kyuquot Sound, along with comparisons between the analytical model and FVCOM.

Chapter 5 discusses and compares the energy conservation in Crowther Channel from FVCOM and the side Channel from the analytical model.

Chapter 6 offers a summary of this thesis and possible routes for further developments.

Chapter 2

Methods

Here, we briefly introduce the model (FVCOM) specifications. Our interest lies in Kyuquot Sound, but the computational domain covers a much larger area (see Fig. 2.2). This large domain is chosen to make sure out point of interest is sufficiently far from the open boundaries where we might have unrealistic solutions. The model is forced by the M_2 tidal constituent elevation along open boundaries, and we assume barotropic conditions (i.e. density, salinity, temperature, wind stress fields are all turned off). The rest of this chapter discusses these setups in more details.

2.1 FVCOM

FVCOM (Chen et al., 2003) (versions 2.7.1 and 3.1.6 were used in this study) provides three-dimensional solutions for flow fields, salinity and temperature in nearshore regions. While finite-difference methods have a general advantage of computational efficiency, their regular grid discretization is not able to accurately fit highly irregular estuarine geometry (Chen et al., 2007), such as in Kyoquot Sound. They also have less flexibility in varying the spatial resolution in subregions where for example, more complex dynamics may warrant smaller grid cells.

FVCOM solves a discretization of the following equations conserving mass, momentum, heat and salt Chen et al. (2003):

Conservation of momentum (Navier-Stokes equations):

$$\frac{\partial u}{\partial t} + u\frac{\partial u}{\partial x} + v\frac{\partial u}{\partial y} + w\frac{\partial u}{\partial z} - fv = -\frac{1}{\rho_0}\frac{\partial P}{\partial x} + \frac{\partial}{\partial z}(K_m\frac{\partial u}{\partial z}) + F_u, \qquad (2.1)$$

$$\frac{\partial v}{\partial t} + u\frac{\partial v}{\partial x} + v\frac{\partial v}{\partial y} + w\frac{\partial v}{\partial z} - fu = -\frac{1}{\rho_0}\frac{\partial P}{\partial y} + \frac{\partial}{\partial z}(K_m\frac{\partial v}{\partial z}) + F_v. \quad (2.2)$$

Hydrostatic approximation:

$$\frac{\partial P}{\partial z} = -\rho(T,S)g. \quad (2.3)$$

Conservation of mass (continuity equation):

$$\frac{\partial u}{\partial x} + \frac{\partial v}{\partial y} + \frac{\partial w}{\partial z} = 0. \quad (2.4)$$

Temperature and salinity advection-diffusion equations :

$$\frac{\partial T}{\partial t} + u\frac{\partial T}{\partial x} + v\frac{\partial T}{\partial y} + w\frac{\partial T}{\partial z} = \frac{\partial}{\partial z}(K_h\frac{\partial T}{\partial z}) + F_T; \quad (2.5)$$

$$\frac{\partial S}{\partial t} + u\frac{\partial S}{\partial x} + v\frac{\partial S}{\partial y} + w\frac{\partial S}{\partial z} = \frac{\partial}{\partial z}(K_h\frac{\partial S}{\partial z}) + F_S, \quad (2.6)$$

where x, y, and z are the east, north, and vertical axes in the Cartesian coordinates; u, v, and w are the corresponding velocity components; S is the salinity; T is the temperature; ρ is the total density that is the sum of the pertubation density ρ' and the reference density ρ_0; P is the pressure; K_m is the vertical eddy viscosity; f is the Coriolis parameter; K_h is the thermal eddy diffusivity; F_u and F_v represent the horizontal momentum diffusion terms; F_T and F_S represent diffusion and source terms [Chen et al., (2003, 2006)].

2.2 Model Setups

Three barotropic model simulation runs for Kyuquot Sound are discussed in this report – r_{20}, r_{21}, and r_{23}. The differences among the simulations are given in Chapter 5. Each simulation is run for 20 M_2 cycles (10.35 days), with a ramp-up time of 2 M_2 cycles, and each cycle has 50 outputs.

The rest of the model setups are listed in detail below.

2.2.1 Location of Interest - Crowther Channel

The Crowther Channel is the location of interest [see (c) in Fig. 2.1], and the entire sound has a complex network of narrow channels and irregular coastal lines. A larger

computational domain [(a) in Fig. 2.2] is chosen so that possible boundary condition inaccuracies would be sufficiently far away enough from the region of interest to not affect results there. The detailed grid layout is discussed in the next section.

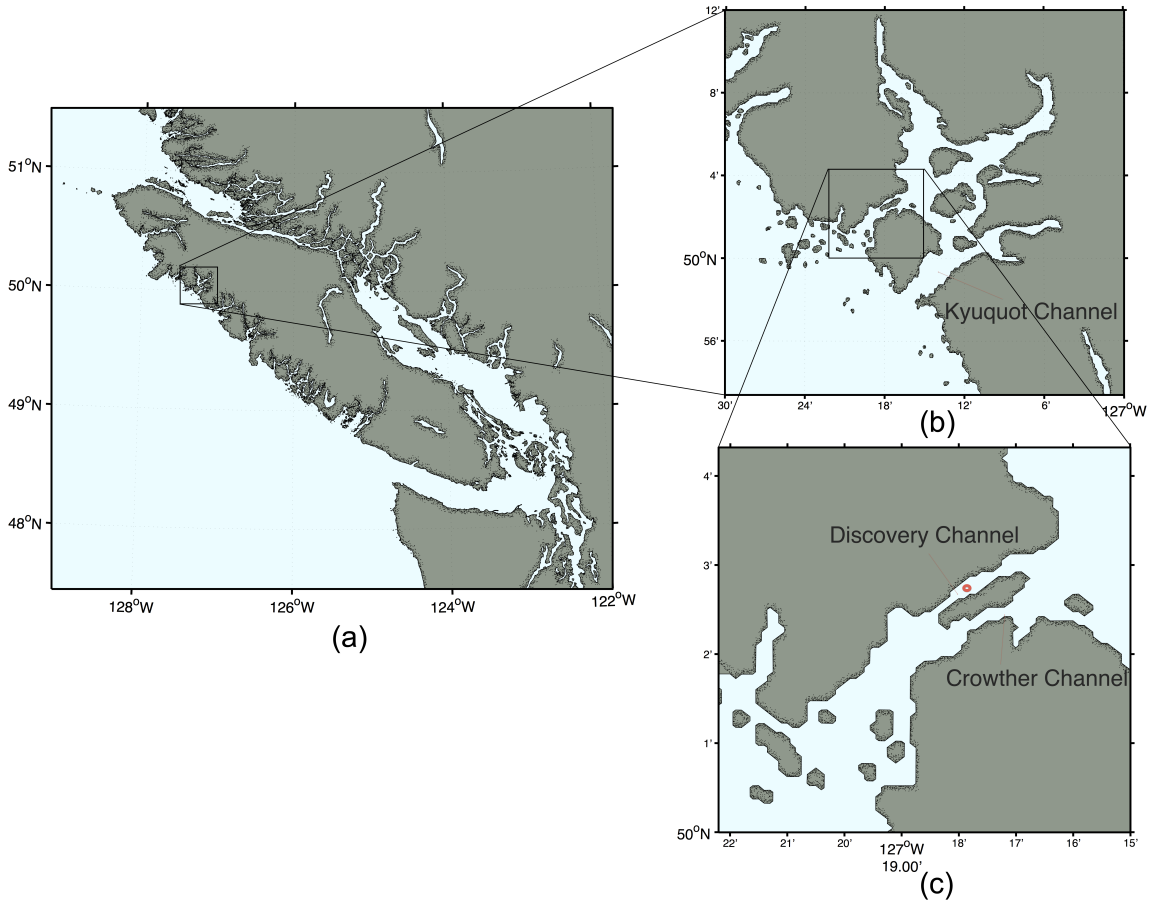

Figure 2.1: Figure (a) is Vancouver Island. (b) is Kyuquot Sound. The red dot in (c) indicates the location of the aquaculture site (approximately 50.05°N 127.30°W) .

2.2.2 Grid Layouts and Discretization

The triangular grid for this simulation has 55, 270 unequally spaced nodes, and 98, 144 triangles horizontally, and 20 vertical σ layers. Horizontally, the irregular triangular grid was generated primarily by Trigrid originally developed by Henry and Walter (1993). The resolution near the aquaculture location is as fine as 10 m (see Fig. 2.2 for the grid map).

FVCOM is a terrain-following model that has the same number of vertical layers everywhere in the domain Chen et al. (2003). The use of the σ-coordinates allow us to rectangularise the vertical grid, making finding derivatives less crumbersome. The σ-coordinate is defined as:

$$\sigma = \frac{z-\eta}{H+\eta} = \frac{z-\eta}{h}, \tag{2.7}$$

where $\eta(x, y, t)$ is the free surface height relative to $z = 0$, $H(x, y)$ is the depth of the bottom, and $h(x, y, t)$ is the total depth. The computational model bathymetry was generated from Canadian Hydrographic Service single-beam digital charts. The bathymetry fields in the computational domain and in Kyuquot Sound are shown in Fig. 2.3 and Fig. 2.4. σ varies from 0 at the surface to -1 at the bottom. The implementation of σ-coordinate system is beneficial when dealing with irregular variable bottom topography (Mellor, 2004). It can potentially cause problems in calculating horizontal advection and dissipation terms (discussed in next chapters) with complex topography, but it provides a better solution to resolving bottom boundary layers. The σ levels that are used in this model have finer resolution near the surface and the bottom to better resolve boundary layers (see Fig. 2.5 for σ level distribution , and Table 2.1 lists the values of σ levels used in the Kyuquot model). The finer bottom resolution helps us resolve the velocity when the bottom friction is in place. Although we do not have any surface stress in this study, the finer surface resolution can be useful when we implement the surface stress in the future.

2.2.3 Initial Conditions and Boundary Forcing

All simulations are started as 'cold start' with 0 velocity, and are forced at the lateral boundaries with M_2 tidal elevations prescribed by amplitudes and phases interpolated from Foreman et al. (2000). Salinity, temperature, freshwater forcing, and wind fields are turned off. The initial density field is uniform and does not change over the course of the simulation ('barotropic mode'), assuming the density field is only contributing to the circulation as a secondary effect. Here we are conducting a sensitivity test of the circulation in a bigger order, so it is safe to assume the density does not play a significant role. The surface boundary stress is zero, and the bottom boundary condition (in terms of bottom stress) is defined as:

$$(\tau_{bx}, \tau_{by}) = C_d \sqrt{u_b^2 + v_b^2}(u_b, v_b), \tag{2.8}$$

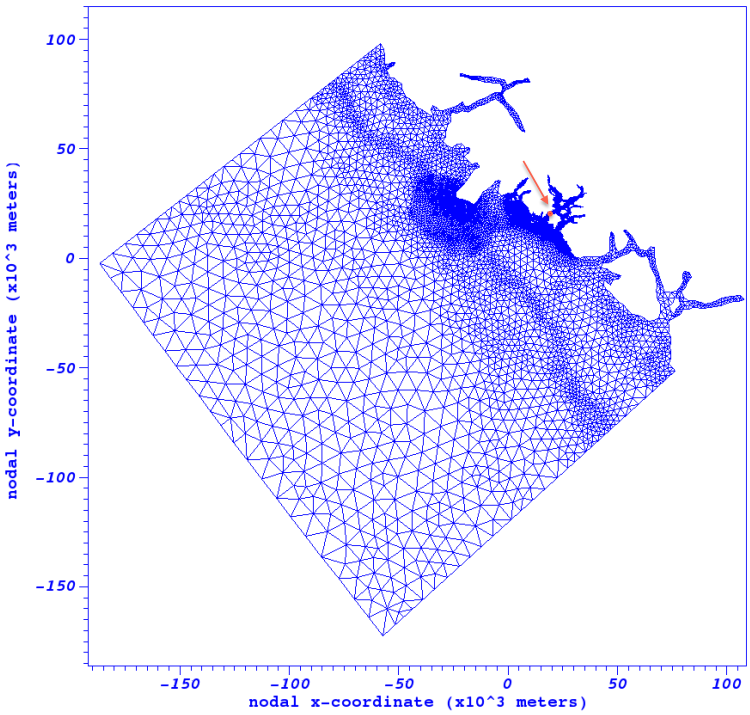

Figure 2.2: The grid of the computational domain, generated by TriGrid. The red dot indicates the location of the aquaculture site 50.05°N 127.30°W, where the resolution is down to 10 m.

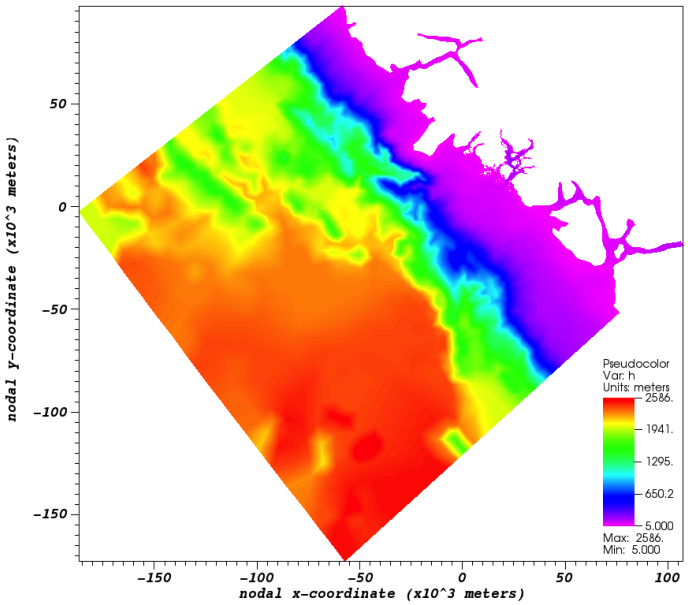

Figure 2.3: Bathymetry for the Computational Domain

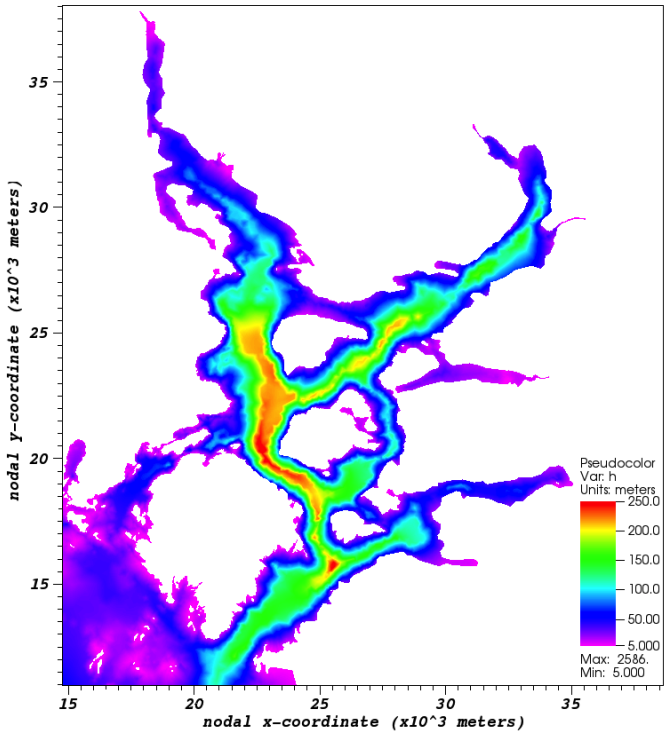

Figure 2.4: Bathymetry in Kyuquot Sound

σ Level	Value	σ Level	Value
1	0.0000000000	11	−0.2693624000
2	−0.0003406892	12	−0.4264195000
3	−0.0010260510	13	−0.6000372000
4	−0.0024033590	14	−0.7520365000
5	−0.0051654530	15	−0.8602291000
6	−0.0106815900	16	−0.9264078000
7	−0.0216065900	17	−0.9632035000
8	−0.0428923400	18	−0.9825834000
9	−0.0830706100	19	−0.9924998000
10	−0.1545639000	20	−0.9974988000
		21	−1.0000000000

Table 2.1: σ Levels for Kyuquot Model Runs

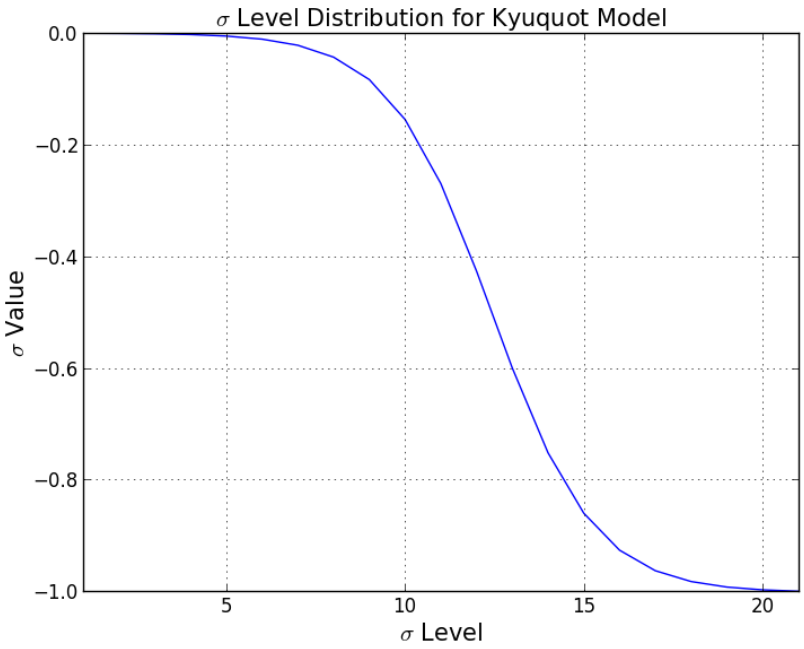

Figure 2.5: Non-uniform σ Level Distribution for Kyuquot Model

where C_d is a user-defined frictional coefficient, (u_b, v_b) is the bottom layer's velocity.

2.2.4 Numerical Stability

Courant-Friedrich Levy (CFL) stability criterion Courant et al. (1967) is a very important necessary condition for numerical stability. However it is not sufficient and previous runs determined the precise time step size used in the runs described here. For consistency purposes, we keep the same computational time step in all our runs. We briefly discuss the numerical stability here, for the sake of completeness

For explicit methods, 1D CFL criterion states:

$$\frac{u\Delta t}{\Delta x} \leq 1, \tag{2.9}$$

where u is the current velocity, Δx is the horizontal grid edge size. If we approximate u with surface gravity wave approximation, we have $u = \sqrt{gh}$. So the external time step is bounded by:

$$\Delta t_E \leq \frac{\Delta L}{\sqrt{gh}}, \tag{2.10}$$

where ΔL is the shortest edge of an individual triangular grid element, and g is the gravitational acceleration.

An exhaustive search for the CFL criteria was performed in the entire domain to calculate the minimum external time step, and $\min(\frac{dL}{\sqrt{gh}})$ was found to be 0.3 s. Our time step in this study (0.0089424 s) is much smaller than this number, ensuring numerical stability across a broad range of forcings.

2.2.5 Vertical and Horizontal Eddy Viscosity Terms

Constant vertical viscosity scheme is used for vertical eddy viscosity parameterization, and either a Smagorinsky closure scheme or constant coefficients methods are used for horizontal eddy viscosity. The details are explained in Chapter 5.

In the next chapter, we present some preliminary results from the Kyuquot Sound model base run, and that leads to a simple analytical model, which represents and can be used to describe dynamics of a two-channel system.

Chapter 3

Response of Kyuquot Sound to Barotropic Tidal Forcing

This chapter provides a general description of results from our Kyuquot Sound model base run (r_{20}). Current circulation is presented for the entire computational domain and the Kyuquot Sound. The complex coastal lines and the bottom topography in Kyuquot Sound lead to some interesting results, especially in term of tidal energy. Special attention is given to the current velocity phases (the concept of phase is introduced in the next section) in Kyuquot Channel and Crowther Channel. The difference in the velocity phases suggests different dynamics in these two channels, and we will discuss the underlying physics in the next chapter.

3.1 Sea Surface Elevation

Pytheas of Marseille around 320 B.C. was one of the first people who documented the rhythmic fall and rise of the sea surface - tides, and it has been serving as one of the most important energy sources in oceans. Tidal analysis requires decomposing tidal signals into various components (constituents) with specified amplitudes and frequencies. M_2 (M_2 is the primary tidal constituent with a period of about 12 hours that is associated with the moon's gravitational force) is the foremost tidal constituent along the Canadian west coast, except a few special places and near Victoria, and it accounts for around 50% of the tidal range (Thomson, 1981).

In the Northeast Pacific Ocean, the Coriolis force and the interaction between the water and the land force the tidal currents to form an amphidromic system with the

amphidromic point located at somewhere between San Diego and Hawaii, and the tide moves counterclockwise around it (Irishab et al., 1971). So tidal waves move northward along the Canadian west coast. The Kyuquot Sound model is forced by an M_2 tidal constituent elevation forcing at the open boundaries. As a first step in validating the model, it is necessary to examine the sea surface elevation response of the tidal forcing over the computational domain and in Kyuquot Sound to see if we can recover the M_2 tide.

The tidal signal propagates as surface gravity waves, and its speed is limited by the shallow water wave speed ($c = \sqrt{gH}$, where g is the gravitational acceleration and H is the bottom depth). Combining the uneven bottom topography and the land that blocks the water from flowing freely, we see a time lag between the maximum forcing and the maximum response. This lag is referred to as the Greenwich phase lag and is a measure of how much the tidal response lags behind the maximum gravitational forcing at the Greenwich meridian (0° longitude) (Pawlowicz et al., 2002). Essentially, the Greenwich phase lag provides a reference to measurethe timing of high or low tide, and computationally it can be estimated by a harmonic tidal analysis.

We used the last two tidal cycles of r_{20} results, conducting a harmonic tidal analysis that is developed by Pawlowicz et al. (2002), who followed the algorithms described by Godin (1972), Foreman (1977), and Foreman (1978). The tidal analysis shows that the M_2 tidal wave is indeed travelling from the south to the north along the coast (see Fig. 3.1a), and the phase of the sea surface elevation is approximately constant (see Fig. 3.1b) over the Kyuquot Sound (less than 1 degree variation). To put these phase values in perspective, 1 hour difference is roughly equal to 29°, and every degree is about 2 minutes for M_2.

The non-tidal quantity (residual that is not explained by the harmonic analysis) of the sea surface elevation is around 0 everywhere in the computational domain (Fig. 3.1d), and this is less than 0.1% of the elevation (the elevation is about 1 m, see Fig. 3.1c for the elevation map). This result indicates that most of the sea surface elevation signal is explained by an M_2 tidal constituent forcing.

3.2 Tidal Currents

While the tidal height is basically in phase throughout the Kyuquot Sound (Fig. 3.2a), the tidal velocities have very different phases, in particular with Crowther and Discovery Channel showing a 90 degree phase difference from Kyuquot Channel(Fig. 3.5).

During the flood tide (Fig. 3.3a) and the ebb tide (Fig. 3.4a) in Kyuquot Channel, it is clear that these currents are forced by the currents in the open ocean, and are much faster than the ones in Crowther Channel and Discovery Channel during flood tide. If we zoom in the Crowther Channel and Discovery Channel region (second figures of Fig. 3.3a and Fig. 3.4a), it appears that currents are almost zero in these two channels. However, if we look at the the currents flow in the middle between the Kyuquot Channel ebb and flood tides, the velocity in the Crowther and Discovery Channels are much larger than in Kyuquot Channel. A phase difference exists between these two channels and the Kyuquot Channel. We will explore this interesting property further in the following section.

3.3 Current Velocity and Sea Surface Elevation Phases

Tides in a channel can be most easily understood as a standing wave, where the phase of the sea surface elevation remains constant along a frictionless rectangular channel at each frequency (Freeland and Farmer, 1980). In most FVCOM simulations, we do not have this ideal situation - frictional effects and uneven topography should cause phase difference along channels. However, the preliminary results from our base run (r_{20}) shows an approximately constant sea surface elevation phase for the M_2 tidal constituent within the sound (see Fig. 3.1b), suggesting that we might be able to represent M2 tidal currents as a standing wave within the sound.

Here, we look at the standing wave property in three channels: Kyuquot Channel, Crowther Channel, and Discovery Channel (Fig. 3.2a). If the friction is small, the sea surface elevation (η) should lag the current by approximately 90° (about 3 hours for M_2 tidal constituent), which is a signature of standing waves. The sea surface reaches the maximum when the current direction is turning from positive to negative (positive being flowing into the sound from the ocean). If this is the case throughout the whole sound, we should expect the same phase lag between the tidal currents and the sea surface height at all three channels. However, this is not what we have observed in Kyuquot Sound (Fig. 3.3 and Fig. 3.3).

We summarize previous plots by considering phase differences. The results (Fig. 3.5) suggest some differences between the phases of sea surface heights and velocities at three channels. In the Kyuquot Channel, we can see the sea surface elevation (η) lags

the current velocity by approximately 90° (1/4 of a cycle). In the other two channels, the sea surface elevations lag the current velocities by approximately 180° (1/2 of a cycle). We use approximated phase here because the phase varies along channel and it has cross channel variations. These numerical results suggest that the frictional forces are not small enough to be ignored in the Crowther and Discovery channels.

Because the behaviour in Crowther and Discovery Channels are similar, to simplify the problem, we combine Crowther Channel and Discovery Channel into one channel, and refer it as Crowther Channel. This simplification allows us to propose a simple analytical 2D two-channel system to analyze the tidal currents and sea surface elevations. In the next chapter, we present the analytical model that helps us understand the role of friction and the dynamics in Kyuquot Sound.

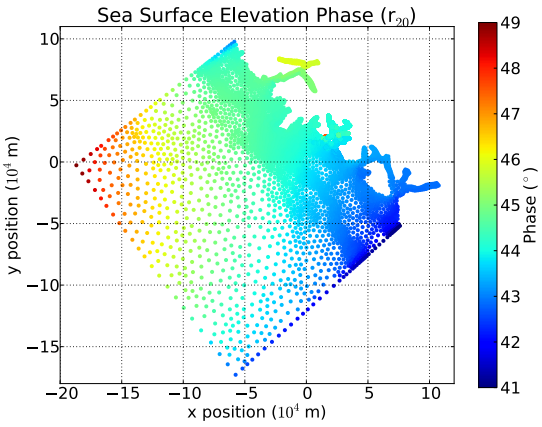

(a) Sea Surface of M_2 Phase Lag (degrees) in the Computational Domain.

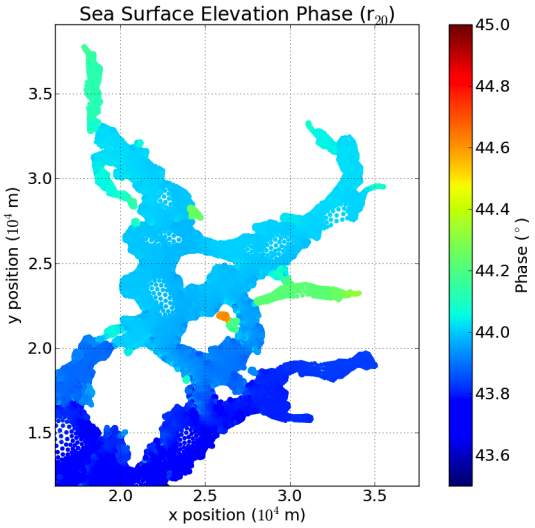

(b) Sea Surface of M_2 Phase Lag (degrees) in Kyuquot Sound.

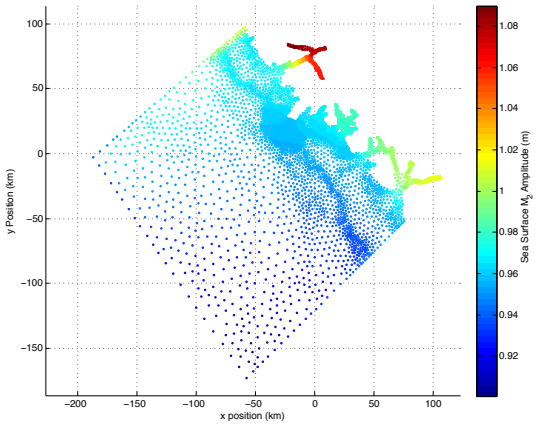

(c) Sea Surface Elevation M_2 Amplitude.

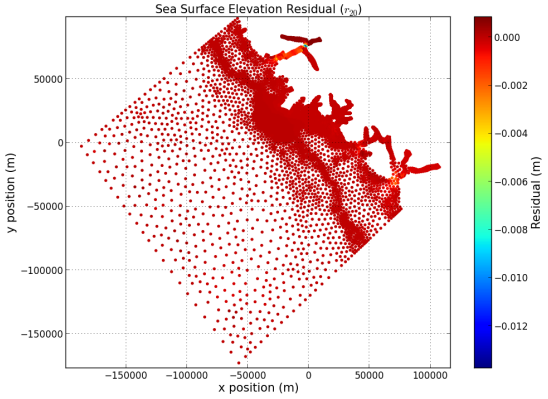

(d) Sea Surface Elevation M_2 Amplitude Residual.

Figure 3.1: Sea Surface T_{tide} Results of the Base Run (r_{20}).

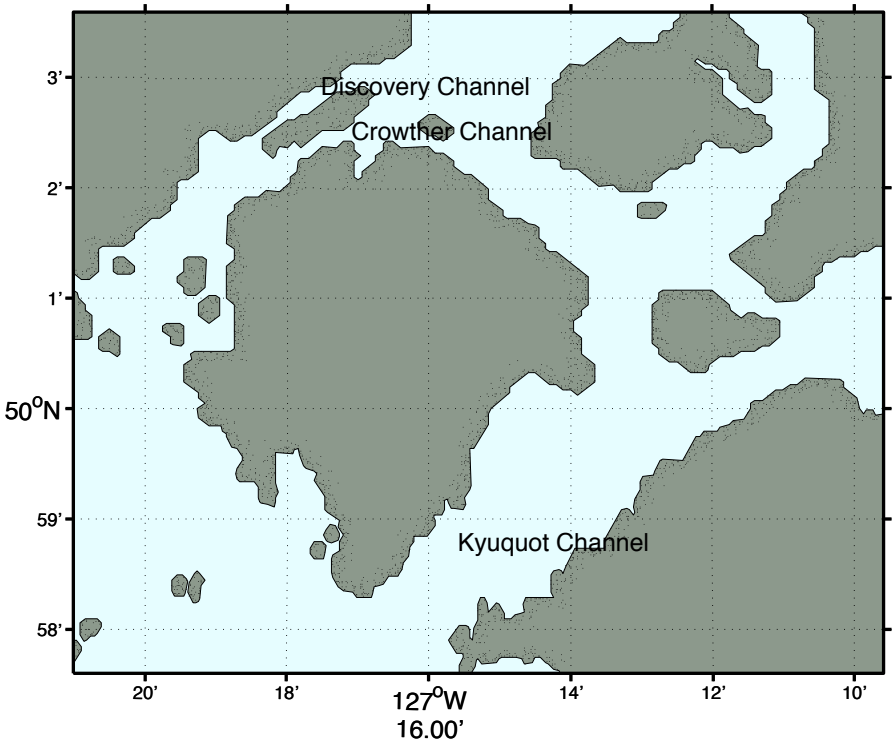

(a) Kyuquot Channel, Crowther Channel, and Discovery Channel.

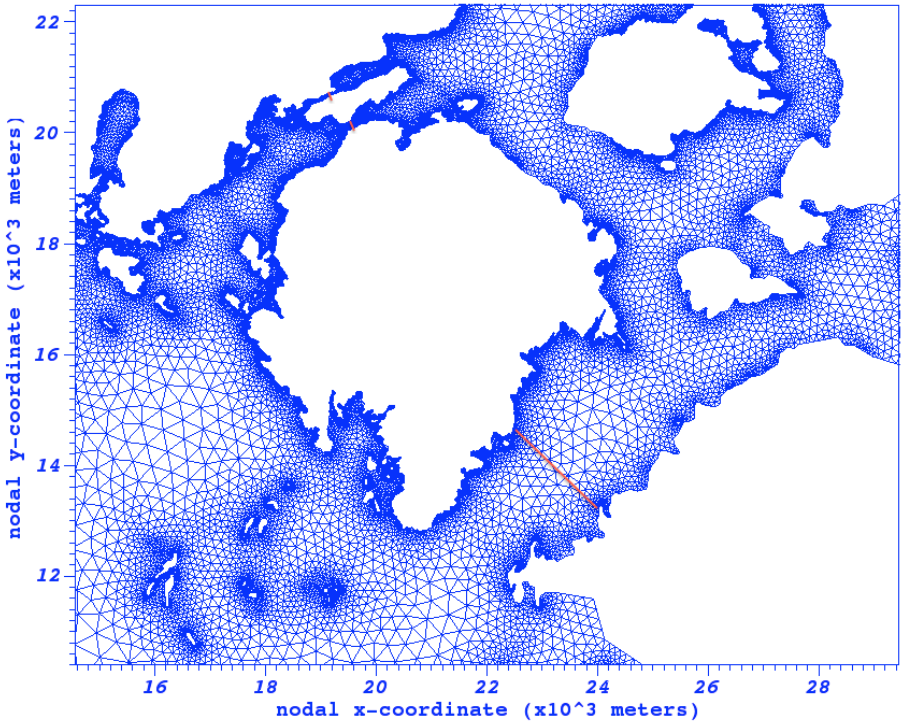

(b) Kyuquot Channel, Crowther Channel, and Discovery Channel Cross Channel Locations. The red lines are locations where normalized velocities and sea surface elevations are examined.

Figure 3.2: Three Channels in Kyuquot Sound

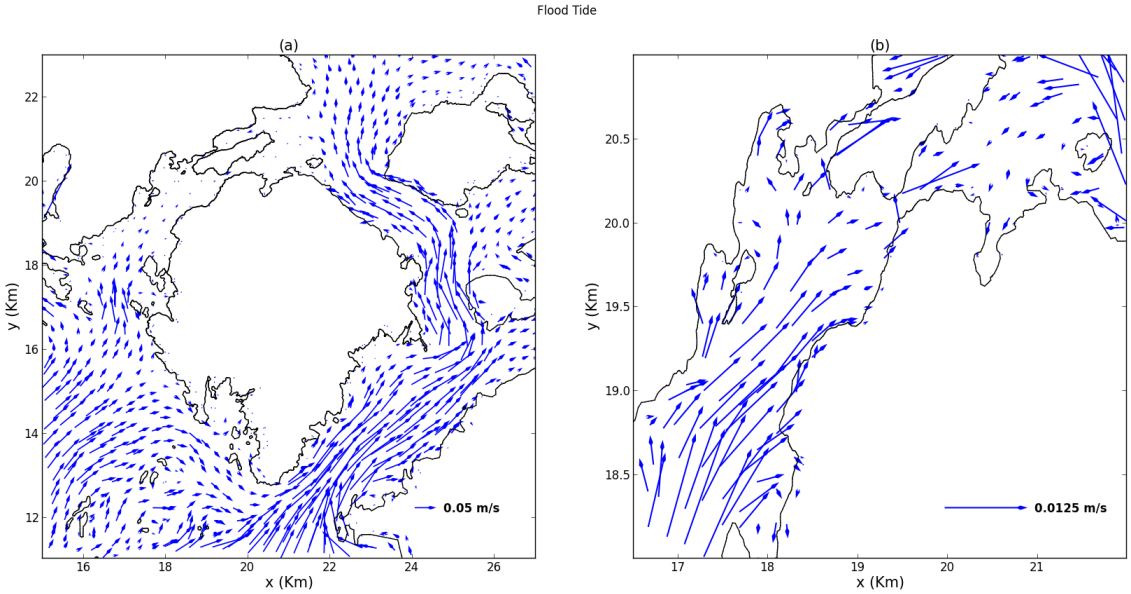

(a) Vertically Averaged Currents at Flood Tide (r_{20}) in Kyuquot Channel.

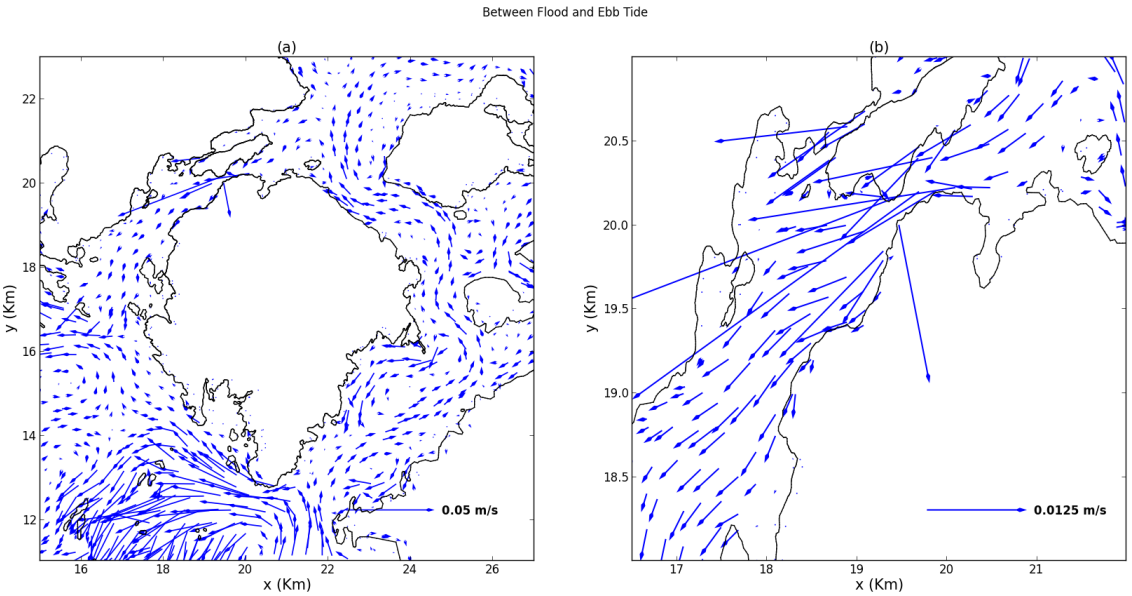

(b) Vertically Averaged Currents Half Way between Flood and Ebb Tide (r_{20}) in Kyuquot Channel.

Figure 3.3: Vertically Velocity Fields in the Base Run (1)

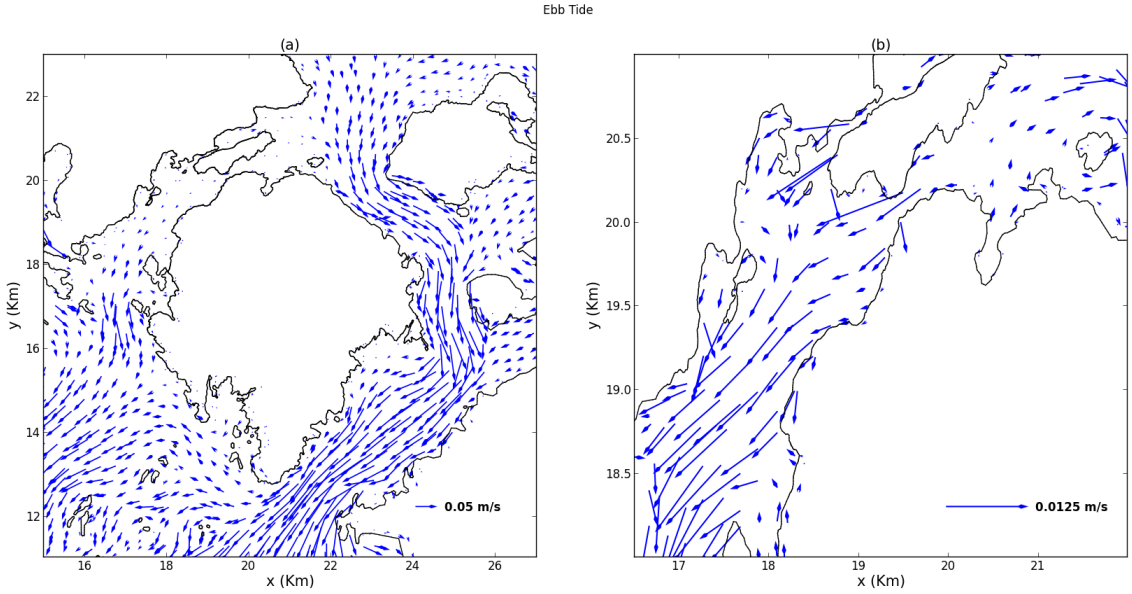

(a) Vertically Averaged Currents at Ebb Tide (r_{20}) in Kyuquot Channel.

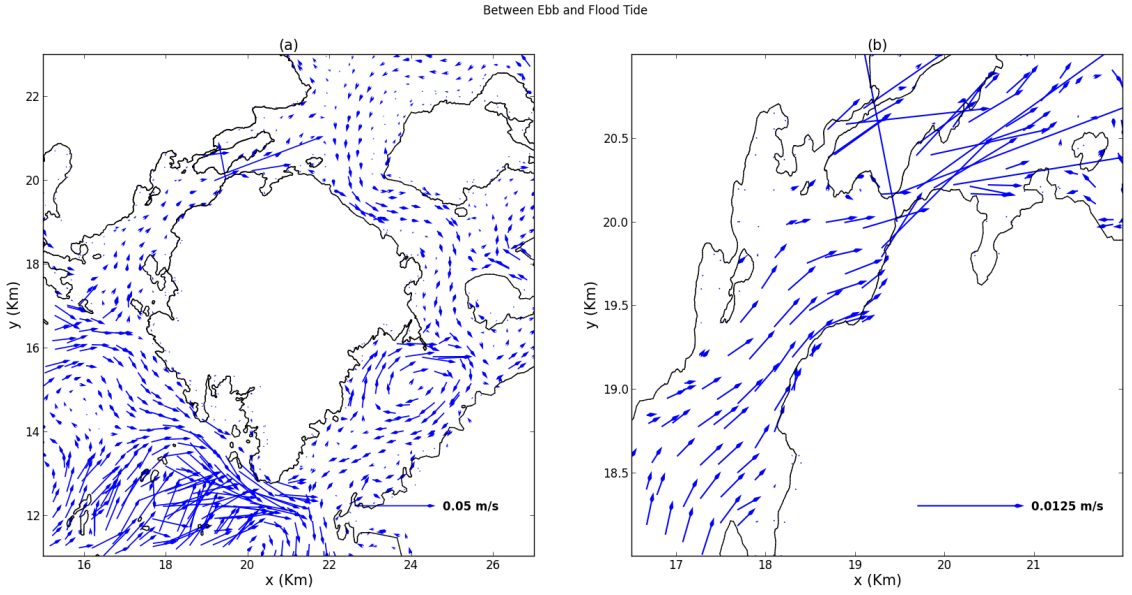

(b) Vertically Averaged Currents Half Way between Ebb and Flood Tide (r_{20}) in Kyuquot Channel.

Figure 3.4: Vertically Velocity Fields in the Base Run (2)

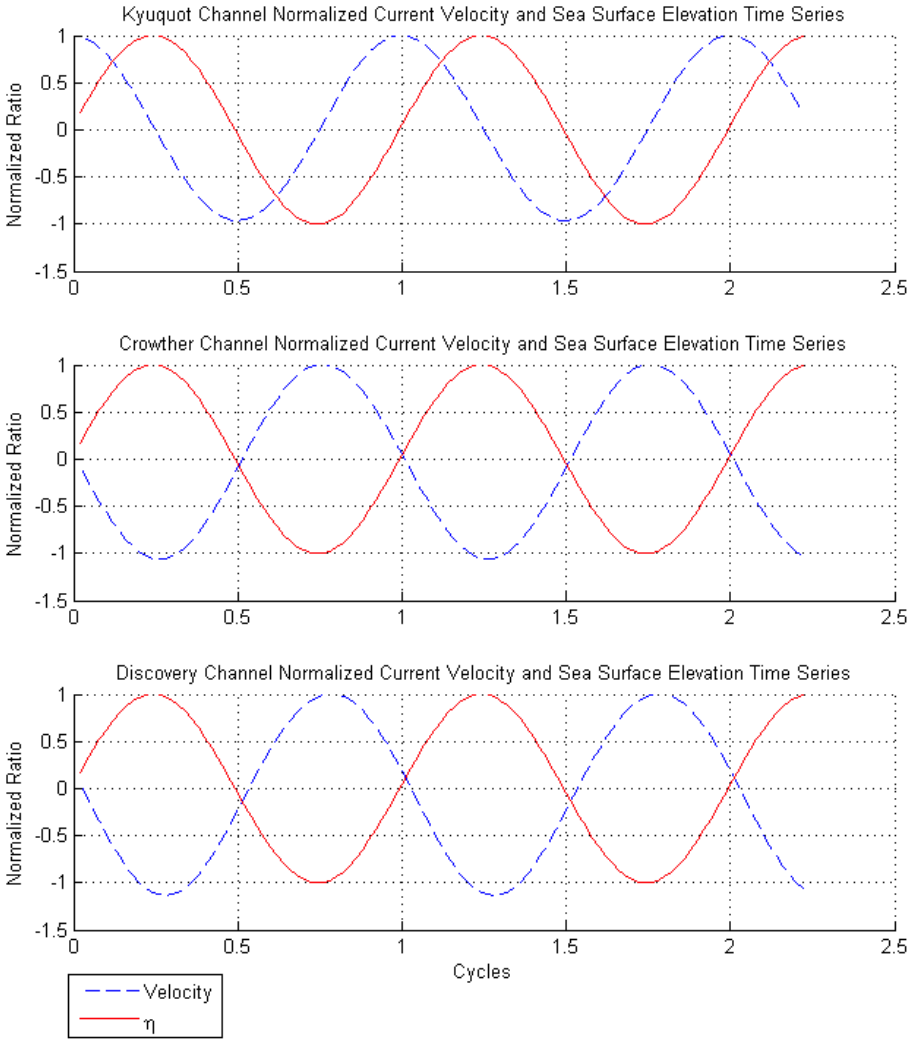

Figure 3.5: Linear Fit of the Normalized Sea Surface Elevation (η) and Current Velocity (50 points/tidal cycle) at mid Three Channels from the Base Run (r_{20}). The locations of these data are taken from the mid-transects (marked in Fig. 3.2b) from the three channels

Chapter 4

Two-Channel System in Kyuquot Sound

In the previous chapter, we looked at the phase lags between current and sea surface elevation in the two channels of Kyuquot Sound qualitatively. Here, we propose an analytical model to quantitatively describe the different dynamics in the two channels, and compare how well the analytical model agrees with the numerical simulation results.

4.1 Model Setup and Assumptions

A 1D model is used to explain the mechanism. To simplify the problem, two channels will be considered. A main channel represents the Kyuquot Channel [Fig. 4.1(a)], and a side channel represents the Crowther Channel [Fig. 4.1(b)]. Point A and C are the ocean ends of the channels; point O is the joint point of the two channels, and B is the end of the main channel.

The dimensions are defined as follows:

- One dimensional flow is assumed;
- $AB = 27,000$ m, $AO = 11,800$ m, and $CO = 6,900$ m;
- Flat uniform depth in each of the channels: $H(AB) = 200$ m, and $h(CO) = 30$ m.

Assume solutions to the horizontal velocity and the sea surface elevation are:

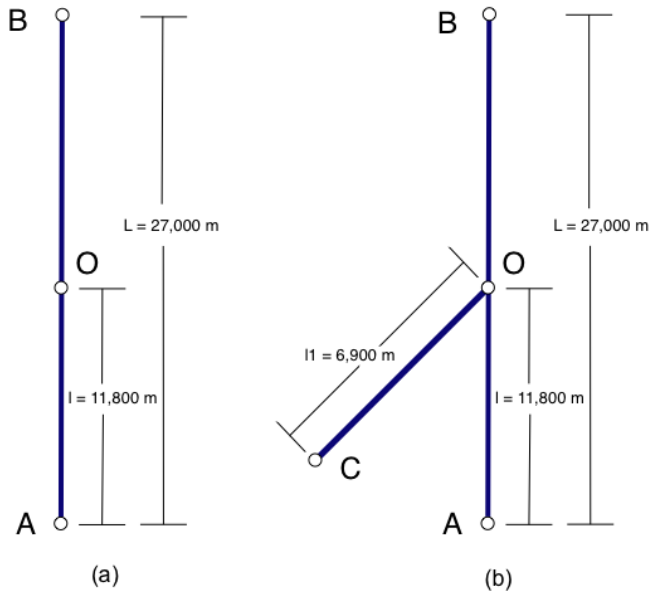

Figure 4.1: The Two Channel System. AB from (a) is the main channel and CO from (b) is the side channel (joining the main channel at point O). The positive directions are from A to B, and from C to O.

$$u = u_0 e^{i(\omega t - kx)} \tag{4.1a}$$

$$\eta = \eta_0 e^{i(\omega t - kx)} \tag{4.1b}$$

where ω is the tidal constituent (driving force) frequency, k is the corresponding wave number, u is the one dimensional current velocity, η is the sea surface elevation, u_0 is the amplitude of the velocity, and η_0 is the amplitude of the sea surface elevation.

The governing equations for the current $u(x,t)$ and the sea surface elevation $\eta(x,t)$ as functions of the position x and time t are the linearized 1D continuity equation and the linearized momentum equation, and taken as:

$$\frac{\partial u}{\partial x} + \frac{1}{H}\frac{\partial \eta}{\partial t} = 0 \tag{4.2}$$

$$\frac{\partial u}{\partial t} + g\frac{\partial \eta}{\partial x} + \frac{r}{H}u = 0 \tag{4.3}$$

where H is the flat bottom depth, g is the gravitational acceleration, and r is a linear

frictional coefficient.

4.1.1 Procedures

u and η are solved in the main channel, assuming that the side channel has little effect on the main channel flow. Once u and η are found for the main channel, boundary conditions $\eta(x = AO)$ and $\eta(x = 0)$ will be used to solve u_1 and η_1 at the side channel. Following these procedures, analytical solutions are obtained and explained in the next section.

4.2 Analytical Solutions with Linearized Friction

4.2.1 Dispersion Relation

Substituting u (Eqn. 4.1a) and η (Eqn. 4.1b) into the continuity equation (Eqn. 4.2) and the linearized momentum equation (Eqn. 4.3), we get the following relations [the same dispersion relation can also be obtained by following Gill (1982)]:

$$\begin{aligned} k_{\pm} &= \pm\sqrt{\frac{\omega^2}{gH} - \frac{ir\omega}{gH^2}} \\ &= \pm\sqrt{\frac{\omega}{gH}}\sqrt{\omega - \frac{r}{H}i} \end{aligned} \tag{4.4}$$

Re-write $k_{\pm}$:

$$\left(\frac{\omega}{gH}\right)^{\frac{1}{2}} \left(\omega - \frac{r}{H}i\right)^{\frac{1}{2}} = k_r e^{i\phi} \tag{4.5}$$

Then we have:

$$k_{\pm} = \pm k_r e^{i\phi} \tag{4.6}$$

where $k_r = \left(\frac{\omega}{gH}\right)^{\frac{1}{2}} \left(\omega^2 + \frac{r^2}{H^2}\right)^{\frac{1}{4}}$, and $\phi = \frac{1}{2}\tan^{-1}\left(\frac{-r}{H\omega}\right)$

Eqn. 4.6 is the dispersion relation when a linear friction term is introduced to the momentum equation. Note that if $r = 0$ (no friction assumption), the dispersion relation is simply $k = \pm\frac{\omega}{\sqrt{gH}}$. $k = k_r e^{i\phi}$ will be used in the next sections.

4.2.2 Main Channel General Solutions with Friction

In the main channel, assume solutions for the time and space dependent sea surface elevation and tidal currents are:

$$u(x,t) = u_0 e^{i(\omega t - kx)} + u_0{}' e^{i(\omega t + kx)} \tag{4.7a}$$

$$\eta(x,t) = \eta_0 e^{i(\omega t - kx)} + \eta_0{}' e^{i(\omega t + kx)} \tag{4.7b}$$

where u_0 is the amplitude of the northward (positive) tidal current, $u_0{}'$ is the amplitude of the southward (negative) tidal current (reflection from the initial tidal current), η_0 is the amplitude of the sea surface elevation of the northward (positive) tidal wave, and $\eta_0{}'$ is the amplitude of the southward (negative) of the sea surface elevation of the tidal wave.

Substituting u and η into the governing equations (Eqn. 4.2) and Eqn. 4.3), we have the following relations:

$$u_0 = \frac{\omega}{kH}\eta_0 \tag{4.8a}$$

$$u_0{}' = -\frac{\omega}{kH}\eta_0{}' \tag{4.8b}$$

Because u is 0 at the end of the channel (point B), and the sea surface elevation at point A is forced by tidal constituent, we have the following boundary conditions:

$$u(L,t) = 0; \tag{4.9}$$

$$\eta(0,t) = \eta_A e^{i(\omega t - \alpha)}, \tag{4.10}$$

where η_A is the sea surface elevation amplitude at point A, and α is the phase.

After applying the boundary conditions and Eqns. 4.8a & 4.8b, we obtain the analytical form of the amplitudes:

$$u_0 = \frac{\omega}{kH}\frac{\eta_A e^{-i\alpha}}{e^{-2ikL}+1} \tag{4.11}$$

$$\eta_0 = \frac{\eta_A e^{-i\alpha}}{e^{-2ikL}+1} \tag{4.12}$$

$$u_0{}' = -\frac{\omega}{kH}\frac{\eta_A e^{-2ikL-i\alpha}}{e^{-2ikL}+1} \tag{4.13}$$

$$\eta_0{}' = \frac{\eta_A e^{-2ikL-i\alpha}}{e^{-2ikL}+1} \tag{4.14}$$

Therefore, the general solutions of $u(x,t)$ and $\eta(x,t)$ are:

$$u(x,t) = \left(\frac{\omega}{kH}\frac{\eta_A e^{-i\alpha}}{e^{-2ikL}+1}\right)e^{i(\omega t-kx)} + \left(-\frac{\omega}{kH}\frac{\eta_A e^{-2ikL-i\alpha}}{e^{-2ikL}+1}\right)e^{i(\omega t+kx)} \tag{4.15a}$$

$$\eta(x,t) = \left(\frac{\eta_A e^{-i\alpha}}{e^{-2ikL}+1}\right)e^{i(\omega t-kx)} + \left(\frac{\eta_A e^{-2ikL-i\alpha}}{e^{-2ikL}+1}\right)e^{i(\omega t+kx)} \tag{4.15b}$$

Simplifications and Approximations of the General Solutions of the Main Channel

It is difficult to understand the dynamics of tidal currents and elevations in the main channel by looking at these general solutions. Some simplifications will help us interpret what exactly the solutions tell us. We can simplify these solutions without loss of generality, by assuming that $\alpha = 0$ and $\eta_A = 1$ (i.e. these are equivalent to setting the sea surface elevation phase at Point A to 0 and the sea surface elevation amplitude to 1 m, so we can look at the phase difference and amplitude relative to Point A):

$$u(x,t) = \left(\frac{\omega}{kH}\frac{1}{e^{-2ikL}+1}\right)e^{i(\omega t-kx)} - \left(\frac{\omega}{kH}\frac{e^{-2ikL}}{e^{-2ikL}+1}\right)e^{i(\omega t+kx)}; \tag{4.16a}$$

$$\eta(x,t) = \left(\frac{1}{e^{-2ikL}+1}\right)e^{i(\omega t-kx)} + \left(\frac{e^{-2ikL}}{e^{-2ikL}+1}\right)e^{i(\omega t+kx)}. \tag{4.16b}$$

Providing the following parameters:

$$L = 27,000 \text{ m} \tag{4.17}$$

$$H = 200 \text{ m} \tag{4.18}$$

$$\omega = 0.0001405257 \text{ rad/s } (M_2 \text{ frequency}) \tag{4.19}$$

$$r = 0.01 \tag{4.20}$$

then we have:

$$k = 3.22 \cdot 10^{-6} - 5.56 \cdot 10^{-7} i \tag{4.21}$$

$$= 3.27 \cdot 10^{-6} \cdot e^{i\theta_k} \tag{4.22}$$

$$e^{-2ikL} = 0.956 - 0.168i \tag{4.23}$$

$$= 0.970 \cdot e^{i\theta_L} \tag{4.24}$$

where $\theta_k = -9.79°$ and $\theta_L = -9.97°$, both of which are small angles. If we approximate $e^{-2ikL} = 1$ and $k = k_r$, we can further simplify the general solutions to:

$$\begin{aligned} u(x,t) &\approx \frac{\omega}{2k_r H}\left(e^{i(\omega t - k_r x)} - e^{i(\omega t + k_r x)}\right) \\ &= \frac{\omega}{k_r H} sin(k_r x)[sin(\omega t) - icos(\omega t)] \\ &= \frac{\omega}{k_r H} sin(k_r x) e^{i(\omega t - \frac{\pi}{2})} \end{aligned} \tag{4.25}$$

$$\begin{aligned} \eta(x,t) &\approx \frac{1}{2}\left(e^{i(\omega t - k_r x)} + e^{i(\omega t + k_r x)}\right) \\ &= cos(k_r x)[cos(\omega t) + isin(\omega t)] \\ &= cos(k_r x) e^{i\omega t} \end{aligned} \tag{4.26}$$

Note that both $\frac{\omega}{k_r H} sin(k_r x)$ and $cos(k_r x)$ are real, so the above simplified results indicate that the sea surface elevation lags the current velocity by $\pi/2$ (90 degrees, suggesting standing wave), which agrees with the numerical results from FVCOM, and this phase lag is independent of x. Moreover, the approximation $k = k_r$ that we made earlier effectively removed the x-dependent phase shifts that could be caused by $sin(k_r x)$ and $cos(k_r x)$ in u and η, respectively. The physical rationale for this approximation is that the wavelength of M_2 tidal constituent is very large (in order of 10^3 km), and $x = [0, L = 27]$ km only comprises a small portion of the wavelength and thus, the sea surface in the sound goes up and down roughly together, which is also in an agreement with the model results (Fig. 3.1b).

4.2.3 Side Channel General Solutions

Now, let us look at the side channel solutions [see Fig. 4.1 (b)] given the solutions found in the main channel from the last section.

Assume solutions for the time and space dependent sea surface elevation and tidal current velocity in the side channel are the real parts of η_1 and u_1 that can be written as :

$$u_1(x,t) = u_{10}e^{i(\omega t - k_1 x)} + {u_{10}}'e^{i(\omega t + k_1 x)} \tag{4.27a}$$

$$\eta_1(x,t) = \eta_{10}e^{i(\omega t - k_1 x)} + {\eta_{10}}'e^{i(\omega t + k_1 x)} \tag{4.27b}$$

where u_{10} is the amplitude of the positive (eastward) current velocity, ${u_{10}}'$ is the amplitude of the reflection of the positive current velocity (negative), η_{10} is the amplitude of the sea surface elevation of the positive direction current, ${\eta_{10}}'$ is the amplitude of the sea surface elevation of the negative direction current, and k_1 is the wave number, at the side channel.

u_1 and η_1 have to satisfy the linearized 1D continuity equation and the linearized momentum equation:

$$\frac{\partial \eta_1}{\partial t} + \frac{\partial (hu_1)}{\partial x} = 0 \tag{4.28}$$

$$\frac{\partial u_1}{\partial t} + g\frac{\partial \eta_1}{\partial x} + \frac{r_1}{h}u_1 = 0 \tag{4.29}$$

where r_1 is the bottom friction coefficient in the side channel, and h is the uniform depth of the side channel.

Substitute u_1 and η_1 into the governing equations (Eqns. 4.28 & 4.29), then we have the following relations between u_1 and η_1 as in the main channel:

$$u_{10} = \frac{\omega}{k_1 h}\eta_{10} \tag{4.30a}$$

$${u_{10}}' = -\frac{\omega}{k_1 h}{\eta_{10}}' \tag{4.30b}$$

The same dispersion relation holds:

$$k_{1\pm} = \pm k_{1r} e^{i\phi_1} \tag{4.31}$$

where $k_{1r} = \left(\frac{\omega}{gh}\right)^{\frac{1}{2}} \left(\omega^2 + \frac{r_1^2}{h^2}\right)^{\frac{1}{4}}$, and $\phi = \frac{1}{2}\tan^{-1}\left(\frac{-r_1}{h\omega}\right)$

Boundary conditions are defined by the sea surface elevations at two ends of the side channel (recap: C is the seaward mouth of the side channel, O is the junction of the side channel with the main channel) . The first boundary condition is the sea surface elevation at Point C in Fig. 4.1 (b) is determined by the amplitude of the elevation. We assume the sea surface phase at Point C in Fig. 4.1 (b) is the same as Point A (Fig. 3.1b suggests this is close to being true). The second boundary condition is that the sea surface elevation at the side channel Point O is the same as the one in Point O calculated from the main channel general solution:

$$\eta_1(0,t) = \eta_C e^{i(\omega t - \alpha)} \tag{4.32}$$

$$\eta_1(l_1,t) = \eta(l,t), \tag{4.33}$$

where $l_1 = 6900m$, and $l = 11,800m$; α is the phase of the tidal constituent, ω is the frequency of the tidal constituent, η is the function of the elevation amplitude in the main channel, and η_C is the sea surface elevation at point C.

Applying boundary conditions to η_1, we get ${\eta_{10}}'$ and η_{10}:

$$\eta_{10} = \frac{\frac{\eta_A e^{-i\alpha}}{e^{-2ikL}+1} e^{-ikl} + \left(\frac{\eta_A e^{-2ikL-i\alpha}}{e^{-2ikL}+1}\right) e^{ikl} - \eta_C e^{i(-\alpha+k_1 l_1)}}{e^{-ik_1 l_1} - e^{ik_1 l_1}} \tag{4.34}$$

$${\eta_{10}}' = \eta_A e^{-i\alpha} - \eta_{10} \tag{4.35}$$

Therefore, the general solutions of u_1 and η_1 in the side channel are:

$$u_1(x,t) = \left(\frac{\omega}{k_1 h} \frac{\frac{\eta_A e^{-i\alpha}}{e^{-2ikL}+1} e^{-ikl} + \left(\frac{\eta_A e^{-2ikL-i\alpha}}{e^{-2ikL}+1}\right) e^{ikl} - \eta_C e^{i(-\alpha+k_1 l_1)}}{e^{-ik_1 l_1} - e^{ik_1 l_1}} \right) e^{i(\omega t - k_1 x)}$$
$$- \left[\frac{\omega}{k_1 h} \left(\eta_A e^{-i\alpha} - \frac{\frac{\eta_A e^{-i\alpha}}{e^{-2ikL}+1} e^{-ikl} + \left(\frac{\eta_A e^{-2ikL-i\alpha}}{e^{-2ikL}+1}\right) e^{ikl} - \eta_C e^{i(-\alpha+k_1 l_1)}}{e^{-ik_1 l_1} - e^{ik_1 l_1}} \right) \right] e^{i(\omega t + k_1 x)} \tag{4.36a}$$

$$\eta_1(x,t) = \left(\frac{\frac{\eta_A e^{-i\alpha}}{e^{-2ikL}+1} e^{-ikl} + \left(\frac{\eta_A e^{-2ikL-i\alpha}}{e^{-2ikL}+1} \right) e^{ikl} - \eta_C e^{i(-\alpha+k_1 l_1)}}{e^{-ik_1 l_1} - e^{ik_1 l_1}} \right) e^{i(\omega t - k_1 x)} + \left[\eta_A e^{-i\alpha} - \left(\frac{\frac{\eta_A e^{-i\alpha}}{e^{-2ikL}+1} e^{-ikl} + \left(\frac{\eta_A e^{-2ikL-i\alpha}}{e^{-2ikL}+1} \right) e^{ikl} - \eta_C e^{i(-\alpha+k_1 l_1)}}{e^{-ik_1 l_1} - e^{ik_1 l_1}} \right) \right] e^{i(\omega t + k_1 x)} \tag{4.36b}$$

Simplifications and Approximations of the General Solutions of the Side Channel

As before, we can simplify the solutions without loss of generality, by assuming that $\alpha = 0$ and $\eta_A = \eta_C = 1$:

$$u_1(x,t) = \left(\frac{\omega}{k_1 h} \frac{\frac{1}{e^{-2ikL}+1} e^{-ikl} + \left(\frac{e^{-2ikL}}{e^{-2ikL}+1} \right) e^{ikl} - e^{ik_1 l_1}}{e^{-ik_1 l_1} - e^{ik_1 l_1}} \right) e^{i(\omega t - k_1 x)} - \left[\frac{\omega}{k_1 h} \left(1 - \frac{\frac{1}{e^{-2ikL}+1} e^{-ikl} + \left(\frac{e^{-2ikL}}{e^{-2ikL}+1} \right) e^{ikl} - e^{ik_1 l_1}}{e^{-ik_1 l_1} - e^{ik_1 l_1}} \right) \right] e^{i(\omega t + k_1 x)} \tag{4.37}$$

$$\eta_1(x,t) = \left(\frac{\frac{1}{e^{-2ikL}+1} e^{-ikl} + \left(\frac{e^{-2ikL}}{e^{-2ikL}+1} \right) e^{ikl} - e^{ik_1 l_1}}{e^{-ik_1 l_1} - e^{ik_1 l_1}} \right) e^{i(\omega t - k_1 x)} + \left[1 - \left(\frac{\frac{1}{e^{-2ikL}+1} e^{-ikl} + \left(\frac{e^{-2ikL}}{e^{-2ikL}+1} \right) e^{ikl} - e^{ik_1 l_1}}{e^{-ik_1 l_1} - e^{ik_1 l_1}} \right) \right] e^{i(\omega t + k_1 x)} \tag{4.38}$$

Providing the following parameters:

$$l = 11,800 \text{ m} \tag{4.39}$$

$$l1 = 6,900 \text{ m} \tag{4.40}$$

$$h = 30 \text{ m} \tag{4.41}$$

$$r_1 = 0.01 \tag{4.42}$$

we have $e^{ik_1 l_1} = 1.051 + 0.08i$. So we can approximate $e^{ik_1 l_1} = 1$ and apply the same approximation in the main channel $e^{-2ikL} = 1$, then we can further simplify the general solutions to:

$$
\begin{aligned}
u_1(x,t) &= \left(\frac{\omega}{k_1 h}\frac{\frac{1}{2}e^{-ikl}+\frac{1}{2}e^{ikl}-e^{ik_1 l_1}}{-2isin(k_1 l_1)}\right)e^{i(\omega t-k_1 x)} + \frac{\omega}{k_1 h}\left(\frac{\frac{1}{2}e^{-ikl}+\frac{1}{2}e^{ikl}-e^{-ik_1 l_1}}{-2isin(k_1 l_1)}\right)e^{i(\omega t+k_1 x)} \\
&= \left(\frac{\omega}{k_1 h}\frac{cos(kl)-1}{-2isin(k_1 l_1)}\right)e^{i(\omega t-k_1 x)} + \frac{\omega}{k_1 h}\left(\frac{cos(kl)-1}{-2isin(k_1 l_1)}\right)e^{i(\omega t+k_1 x)} \\
&= \left(\frac{\omega}{k_1 h}\frac{cos(kl)-1}{-2isin(k_1 l_1)}\right)\left[e^{i(\omega t-k_1 x)}+e^{i(\omega t+k_1 x)}\right] \\
&= \left(\frac{\omega}{k_1 h}\frac{cos(kl)-1}{-2isin(k_1 l_1)}\right)2cos(k_1 x)e^{i\omega t} \qquad (4.43)
\end{aligned}
$$

$$
\begin{aligned}
\eta_1(x,t) &= \left(\frac{\frac{1}{2}e^{-ikl}+\frac{1}{2}e^{ikl}-e^{ik_1 l_1}}{-2isin(k_1 l_1)}\right)e^{i(\omega t-k_1 x)} - \left(\frac{\frac{1}{2}e^{-ikl}+\frac{1}{2}e^{ikl}-e^{-ik_1 l_1}}{-2isin(k_1 l_1)}\right)e^{i(\omega t+k_1 x)} \\
&= \left(\frac{cos(kl)-1}{-2isin(k_1 l_1)}\right)2sin(k_1 x)e^{i(\omega t-\frac{\pi}{2})} \qquad (4.44)
\end{aligned}
$$

Here, $k_1 = 1.10\cdot 10^{-5} - 7.27\cdot 10^{-6} i$ ($\phi_1 = -33^\circ$), so the coefficients of the exponentials in both u_1 and η_1 are not simple real numbers. What is also important here is that the x-dependent components for u_1 and η_1 are $cos(k_1 x)$ and $sin(k_1 x)$, respectively. Because k_1 is a complex number with phase -33°, the direct results (as will be seen in the next section) are that $sin(k_1 x)$ varies with x more in the imaginary component, and $cos(k_1 x)$ varies more in the real component. In addition, u_1 and η_1 are real physical variables, so $cos(k_1 x)$ provides a bigger x dependency, and this explains why we see an along-channel phase difference in velocity, but not in the sea surface elevation. The phase changes associated with these complex coefficients are discussed further in the next section.

4.3 Results and Discussion

4.3.1 Analytical Solutions vs. FVCOM Results

The analytical solutions derived from the linearized momentum equation and 1D continuity equation are now compared against the numerical solutions from FVCOM in this section.

The numerical FVCOM results are from M_2 tidal constituent forcing only with barotropic condition (uniform salinity and temperature fields throughout the computational domain). As indicated in the first section, the signature of standing waves is only present in the Kyuquot Channel (the main channel); the phase difference be-

tween the velocity and the sea surface elevation is not 90° at the Crowther Channel (the side channel). The phase of the velocity decreases from the western end to the eastern end of the Crowther Channel (see Fig. 4.4) The tide becomes later from the east to west suggesting that the energy enters from the east end (Kyuquot Channel, the main channel) rather than from the west end of the Crowther Channel.

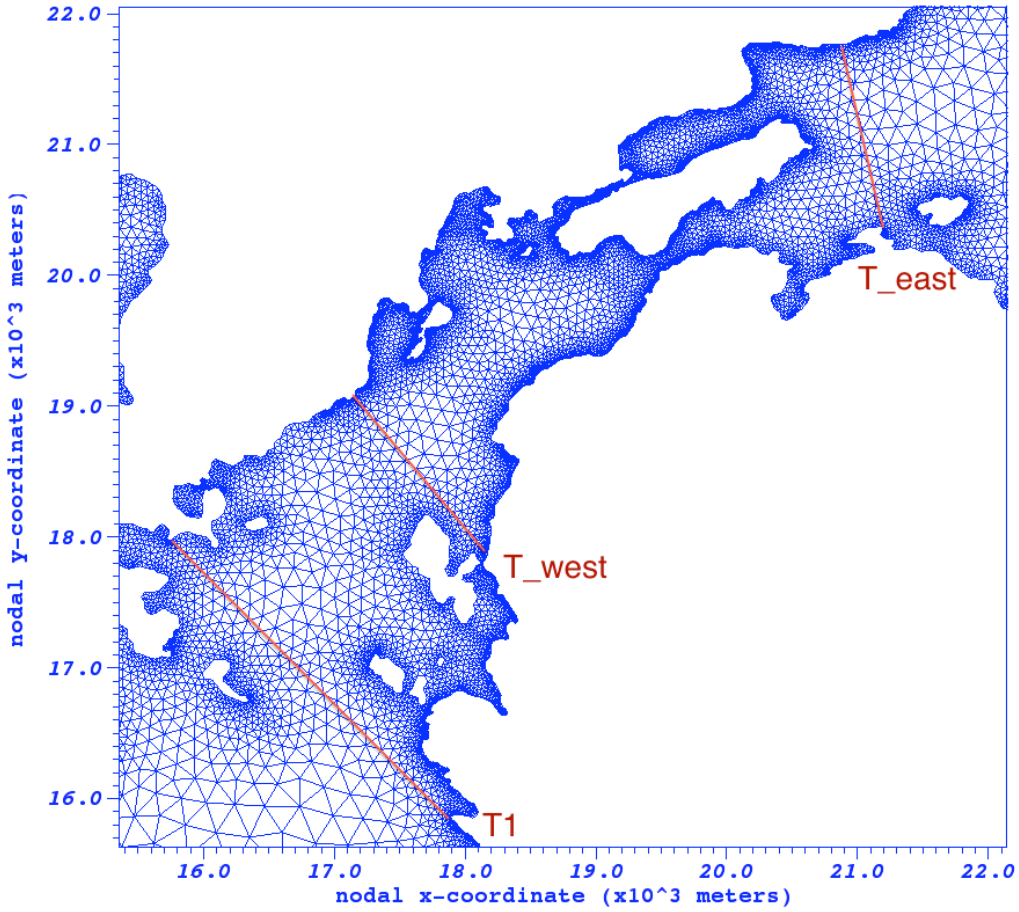

Figure 4.2: Crowther Channel Transect Map. T1 is the left most transect location and T_{east} is the right most transect location.

The analytical solutions of the two channel system showed the same trend as the numerical results (see Fig. 4.5). The phase of velocity at the side channel decreases from the west to east (i.e. varies spatially), while the phase remains the same along the main channel. Two lines of the side channel velocity phase are shown in the plot for $r_1 = 0.006$, and $r_1 = 0.007$. The phase difference gets bigger along the side channel as we increase the frictional coefficient ($r_1 = 0.007$ v.s. $r_1 = 0.006$), suggesting that more energy is lost while we increase the frictional coefficient in the side channel,

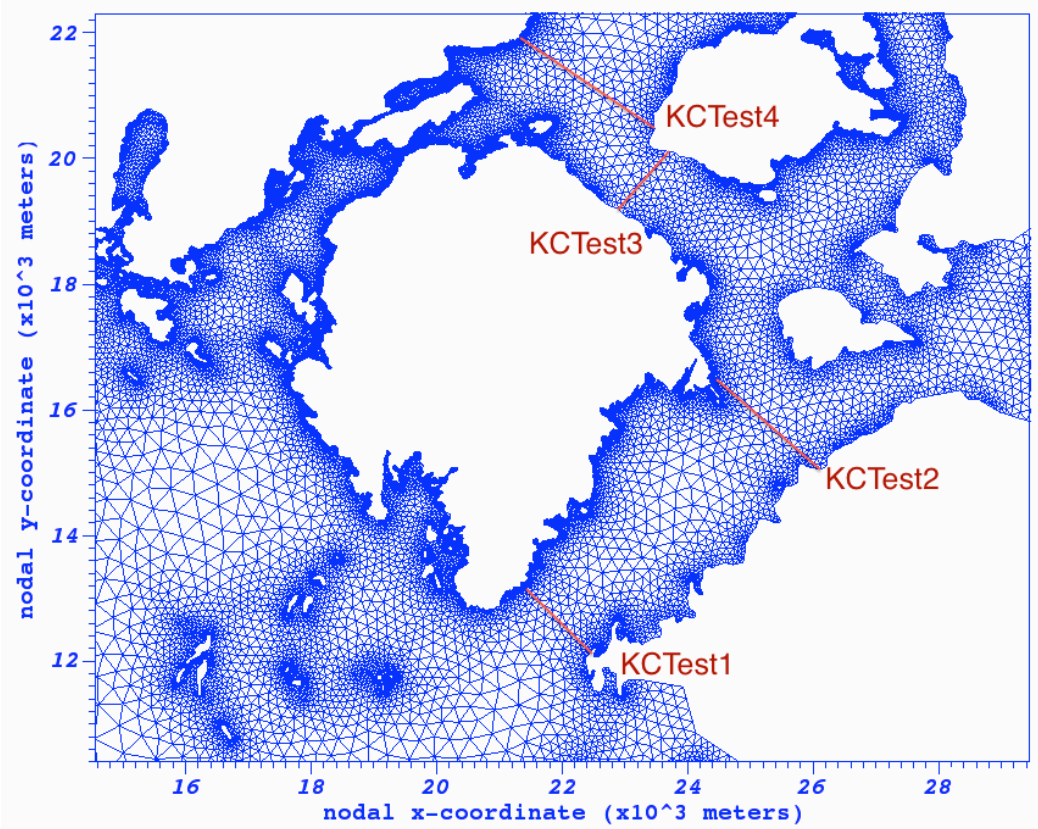

Figure 4.3: Kyuquot Channel Transect Map

which is also what we expect. We could use an optimization method to find the 'best fit' for the frictional coefficients, but it is beyond the scope of this section. In the next section, we discuss how this phase difference occurs and why there is a difference between the behaviours of the main channel and the side channel.

4.3.2 Role of Friction

Sverdrup explained the effects of friction on tidal currents: when the friction is introduced to the flow, the amplitude and the phase of the tidal currents will be modified by the friction subjected to the water, and the phase will vary along the channel (Sverdrup, 1942). The phase difference that we have observed in the analytical model comes from friction.

If the above is true in our case, the phase change should disappear when friction is absent. Setting $r = 0$ and $r_1 = 0$, the solutions in the main channel and the side channel have the same expression but with real k and k_1. The real wave numbers

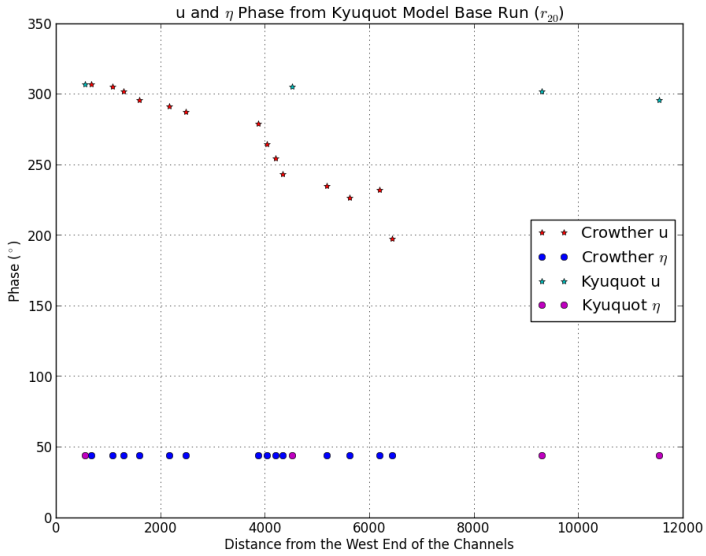

Figure 4.4: Velocity and Sea Surface Elevation Phase Plot from FVCOM Base Run (r_{20}). The points on Crowther Channels are 14 mid-channel u and η phase of from transect T_{west} to T_{east} (see Fig. 4.2). The points in Kyuquot Channels are 4 mid-channel u and η phase of from transect KCTest1 to KCTest4 (see Fig. 4.3).

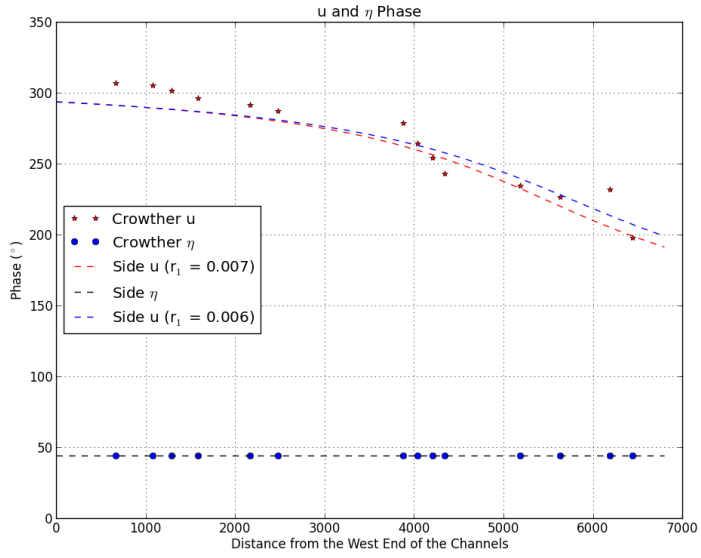

Figure 4.5: Velocity and Sea Surface Elevation Phase Plot from the Side ChannelAnalytical General Solutions and Base Run (r_{20}). Two different r's are used to compute the analytical phase results (note: $r = r_1$).

eliminate the x dependent part in the phase expression, so the velocity phase variation along the side channel disappears after we set the friction coefficients to zero in both channels (see Fig. 4.6). Once the flow is made frictional, a difference of the velocity phase between the western and the eastern ends can be observed in the side channel as what we have seen earlier.

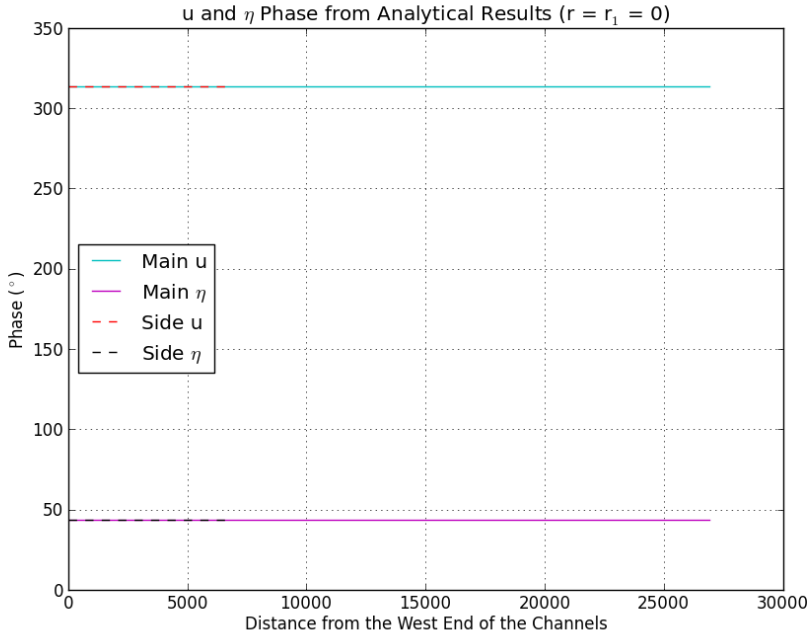

Figure 4.6: Velocity and Sea Surface Elevation Phase Plot from the Analytical Solutions with Zero Friction

A phase difference along channel is not observed in the main channel (Kyuquot Channel) from either the analytical solutions or the FVCOM results. The bottom friction can only influence to a certain distance from the boundary at the bottom, and the influence is very small for the entire body of water if the depth of the channel is large ($H = 200$ m in the main channel). The friction term plays a role in term of r/H, so the friction effects are different when the same frictional coefficient but different depths are given in two channels. If we set the depth in the side channel to $h = H = 200$ m, the phase variation in the side channel is no longer observed (Fig. 4.7). This explains why we do not see a phase variation along the main channel from the analytical results or along the Kyuquot Channel from the FVCOM results.

Friction is a type of energy sink and the presence of friction produced the present

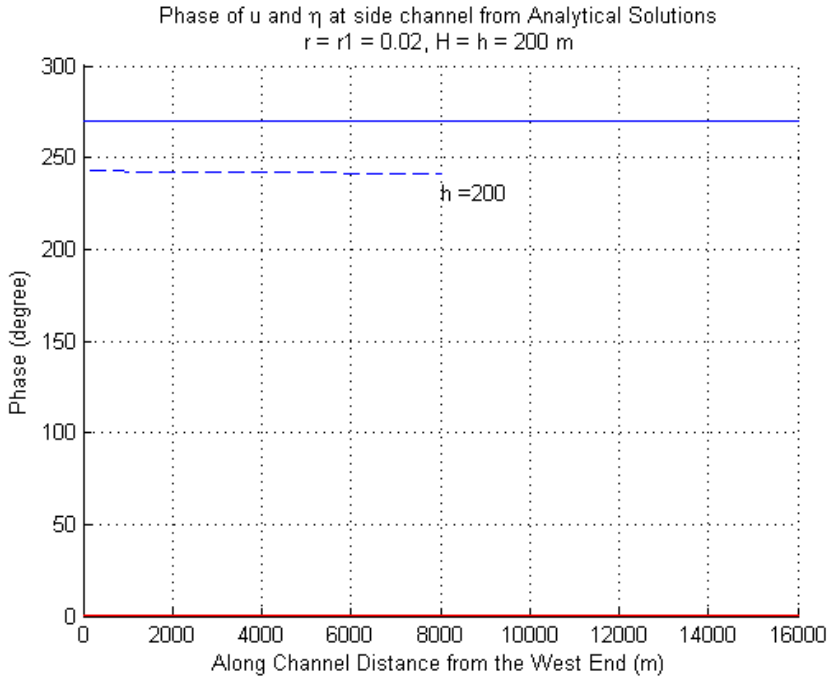

Figure 4.7: Velocity and Sea Surface Elevation Phase Plot from the Analytical Solutions Assuming Same Depths for Both Channels. The blue dashed (solid) line is the side (main) channel elevation, and the red dashed (solid) line (the dashed line is embedded in the solid line) is the velocity in the side (main) channel.

phase change. It is natural to relate the energy loss in the side channel to the velocity phase variations. In the next chapter, we will explore this interesting finding further in detail.

Chapter 5

Energy Budget in Crowther Channel

In the last chapter, we demonstrated linear bottom friction could change the behaviour of the circulation in Kyuquot Sound via simplified analytical model, and we qualitatively compared the phase change between the analytical model and FVCOM numerical results. Here we demonstrate that the energy loss implied by the analytical model is a reasonable approximation to the energy lost in the side channel.

In this chapter, we identify different components in the energy budget of the Crowther Channel from FVCOM simulation results, and compare the energy loss with what the simplified model predicts. It is not trivial to calculate energy budget from FVCOM results, so we follow these steps to formulate the energy balance and to accomplish our energy comparisons:

- **Test Channel**: The complexity of the bottom topography and the coastal lines of the Crowther Channel makes it difficult to determine the source of energy loss. We create a test channel (i.e. Channel1), which is a flat bottom, rectangular channel, as our reference channel.

- **Volume Budget**: It is almost impossible to balance energy if we cannot balance volume. We calculate the volume budget within a section of the channels in Channel1 and in Crowther Channel to establish a 'baseline' for the energy budget uncertainties.

- **Energy Budget**: We formulate energy budget equations, obtain energy balance of Channel1 and Crowther Channel. Then we compare the energy loss

from the Crowther Channel simulations with the energy loss calculated from the simplified analytical model.

5.1 Test Channel and Simulation Overview

We introduce the test channel; Channel1, in this section, and briefly lay out 3 Channel1 model runs and 3 Kyuquot Sound model runs.

5.1.1 Channel1

A rectangular grid, Channel1, is used for testing purposes. Horizontally, there are $19,436$ triangles, and $10,007$ nodes. It is 20 km from the west to the east end (from -10 km to $+10$ km), and 3 km from the south to the north end (from 0 km to 3 km), Vertically, there are ten (10) equally spaced σ-layers, over a uniform depth - 30 m. Open boundaries are at the west and east ends of the channel, and closed boundaries are at the north and south ends (land).

The simulations are run in barotropic mode, and forced by one major semi-diurnal (M2) tidal constituent: sea surface elevations' amplitudes and phases are specified at the open boundaries (left side and right side in this case). The difference in phase values is calculated by shallow water approximation (i.e. the phase speed $= \sqrt{gH}$).

5.1.2 Model Runs

Six simulations runs are analyzed in this chapter. 3 runs (r_4, r_5 and r_6) are for Channel1, and 3 runs (r_{20}, r_{21} and r_{23}) are for Kyuquot Sound. We have given a general overview about the model parameters and output time intervals for Kyuquot Sound in Chapter 2. To keep the results consistent, we also have 50 model outputs per M_2 cycle for Channel1 simulation, and each simulation was run for 20 M_2 cycles. Here we compare the differences among simulation runs in both Channel1 and Kyuquot Sound models.

Channel1:

In Channel1 simulations, Smagorinsky eddy parameterization method is used to determine the horizontal eddy viscosity terms. The same eddy coefficient is chosen for all 3 simulations of Channel1 [$A_m = 0.02\ m^2/s$ (HORCON in FVCOM)]. Vertically, MY-2.5 turbulent parameterization model is implemented in FVCOM ($K_m = 10^{-5} m^2/s$

is the vertical eddy viscosity coefficient). Because we have turned off the wind stress field, the only boundary conditions for the vertical eddy viscosity term is the bottom stress Chen et al. (2003):

$$(\tau_x, \tau_y) = C_d \sqrt{u_b^2 + v_b^2} \tag{5.1}$$

The differences among 3 runs of Channel1 lie in the vertical friction coefficient, C_d (see Table 5.1).

run	C_d [m/s]
r_4	0.0025
r_5	0.0100
r_6	0.1000

Table 5.1: Different Vertical Friction Coefficients used in r_4, r_5 and r_6 of the Channel1 Model Runs.

Kyuquot Sound:
Three barotropic model simulation runs of the Kyuquot Sound are discussed here: r_{20}, r_{21}, and r_{23}. Constant ($k_m = 0.02$ m^2) vertical eddy viscosity coefficient is used for all three runs. The differences among them are in the parameterizations of the horizontal eddy viscosity forcing $\mathcal{F}$. The parameterizations of the horizontal eddy viscosity forcing were suggested by Mellor and Blumberg (1985) in σ-coordinates to achieve higher resolution at bottom boundary layers on irregular slopes without introducing complicated equations when dealing with derivatives. These approximations are:

$$\mathcal{F} = (\mathcal{F}_x, \mathcal{F}_y) \tag{5.2}$$

$$\mathcal{F}_x = \frac{1}{h}\left\{\frac{\partial}{\partial x}\left(2A_m H\frac{\partial u}{\partial x}\right) + \frac{\partial}{\partial y}\left[A_m H\left(\frac{\partial u}{\partial y} + \frac{\partial v}{\partial x}\right)\right]\right\} \tag{5.3}$$

$$\mathcal{F}_y = \frac{1}{h}\left\{\frac{\partial}{\partial x}\left[A_m H\left(\frac{\partial u}{\partial y} + \frac{\partial v}{\partial x}\right)\right] + \frac{\partial}{\partial y}\left(2A_m H\frac{\partial v}{\partial y}\right)\right\} \tag{5.4}$$

where A_m is the horizontal eddy viscosity coefficient.

Constant A_m is used for r_{20} model run:

$$A_m = 20 \text{ m}^2/\text{s}. \tag{5.5}$$

The turbulent Smagorinsky closure parameterization method for horizontal diffusion is used for r_{21} and r_{23} model runs:

$$A_m = 0.5C\Omega^n \sqrt{\left(\frac{\partial u}{\partial x}\right)^2 + 0.5\left(\frac{\partial v}{\partial x} + \frac{\partial u}{\partial y}\right)^2 + \left(\frac{\partial v}{\partial y}\right)^2}, \tag{5.6}$$

where C is a user-defined constant parameter and Ω^n is the area of the individual control element. Different Cs are used for r_{21} and r_{23}:

$$C_{21} = 5.0; \tag{5.7}$$

$$C_{23} = 1.0. \tag{5.8}$$

The differences among the three runs are summarized in Table 5.2.

run	Constant A_m [m^2/s]	Smagorinsky Closure C	max (x-dir) velocity at T$_{west}$) m/s
r_{20}	20.0		0.0091
r_{21}		5.0	0.0195
r_{23}		1.0	0.0279

Table 5.2: Differences of Horizontal Eddy Viscosity Parameterization Scheme in r_{20}, r_{21}, and r_{23}. A_m is the constant horizontal eddy viscosity coefficient used in r_{20} , and C is a user-defined coefficient for the turbulent Smagorinsky closure parameterization method used in r_{21} and r_{23}. Note that a typical value for the coefficient C is around 1.0, and $C = 5.0$ provides a generally smaller A_m than what is used in r_{20} (20.0) in Crowther Channel. So if we compare A_m, r_{20} has the biggest coefficient, and r_{23} has the smallest among these three runs. The last column is a reference to the velocity, showing that the velocity increases in the channel from r_{20} to r_{23}.

Now, let us look at the volume budget with these runs introduced above.

5.2 Volume Conservation

In this section, we examine volume conservations to establish a 'baseline' for the energy budget. The finite-volume technique used in FVCOM discretizes integral forms of the governing equations and solves them by flux calculation, so this approach should provide better accuracy in mass conservation than finite-difference methods (Chen et al., 2006). The flux calculation implements a second-order accurate finite-volume method (Chen et al., 2003), combining with a vertical velocity adjustment to enforce theoretically exact volume conservation in both individual control volumes and the global domain.

The mass conservation can be examined by balancing the difference between influx and outflux volume with the change of the sea surface elevation within a controlled domain in a channel. If we let the controlled channel section have two open boundaries (T_{west} and T_{east}) to allow currents flow in and out, the transport Q in m^3/s (Q_{west} and Q_{east}, respectively) at the transect surface averaged over time ΔT is defined as:

$$\overline{Q(x,t)} = \overline{\int_S u(x,t) \cdot ds} \tag{5.9}$$

where S is the cross-sectional area of the transect, u is the velocity at the transect, x is the position of the transect, and the overbar denotes the time average ($\Delta T = t_f - t_i$) of a function:

$$\overline{f} = \frac{1}{\Delta T} \int_{t_i}^{t_f} f dt. \tag{5.10}$$

The difference between the average transports at two transects should be balanced by the volume change in the controlled domain:

$$\Delta Q + \frac{dV}{dt} = 0, \tag{5.11}$$

where $\Delta Q = Q_{east} - Q_{west}$, and V is total volume in the controlled domain.

Applying the trapezoidal method in discrete form, the imbalance of the volume budget averaged over time ΔT is defined as:

$$Q_{ib} = (\overline{Q}_{east} - \overline{Q}_{west}) + \frac{V(t_f) - V(t_i)}{\Delta T}, \tag{5.12}$$

given that:

$$\overline{Q}_{west} = \frac{1}{\Delta T} \sum_{n=1}^{N} \frac{Q_{n,west} + Q_{n+1,west}}{2} \frac{\Delta T}{N} \tag{5.13}$$

$$\overline{Q}_{east} = \frac{1}{\Delta T} \sum_{n=1}^{N} \frac{Q_{n,east} + Q_{n+1,east}}{2} \frac{\Delta T}{N} \tag{5.14}$$

$$V(t) = \sum_{i=1}^{M} s_i \cdot h_i(t) \tag{5.15}$$

$$\Delta T = t_f - t_i \tag{5.16}$$

where N is the number of equally spaced time steps within time ΔT, M is the number of elements (triangles) in the controlled domain, s_i is the area of the i^{th} element, and $h_i(t)$ is the sea surface elevation of the element column at time t.

Now, we can examine the volume budget in Channel1 and in Crowther channel by evaluating Q_{ib} and we quantify the imbalance by two measures: (1) Q_{ib}/V_{total} in 1/s as the volume change per second in the channel (V_{total} is the total volume of the controlled domain) to show how long it takes to drain the channel if the imbalance persists; (2) Q_{ib}/S_{total} (S_{total} is the total area of the bottom) in m/s as the sea surface change per second due to the imbalance to show how long it takes for the sea surface elevation to change, say 1 mm, if the imbalance persists.

5.2.1 Volume Conservation in Channel1

In Channel1, we set up the controlled domain with two transects as the open boundaries (T_{west} and T_{east}), and let T_{west} be from $(x, y) = (-7,000m, 0m)$ to $(x, y) = (-7,000m, 3,000m)$, and T_{east} be from $(x, y) = (7,000m, 0m)$ to $(x, y) = (7,000m, 3,000m)$. Because we have 20 cycles at 50 storages per cycle, there are 1000 time points. Assuming the last cycle is the closest to steady state in the simulation, we set t_f to be the 999^{th} output and t_i to be the 949^{th} output (i.e. $T = T_{M_2}$). From T_{west} to T_{east}, there are $13,528$ triangles in the rectangular channel (total area is $4.17 \cdot 10^7 m^2$), which

gives us the total volume in the controlled domain:

$$V_{total} = S \cdot D \tag{5.17}$$
$$= 4.17 \cdot 10^7 m^2 \cdot 30m \tag{5.18}$$
$$= 1.251 \cdot 10^9 m^3 \tag{5.19}$$

The volume budget is summarized in Table 5.3. While the volume seems not perfectly balanced, the discrepancy is extremely small compared to the total volume in the channel and the net transport at either end of the channel. Also, if we look at the ratio column, the imbalance Q_{ib} over V_{total} is in the order of 10^{-9} /s. This indicates that if the imbalance persists for 10^9 s (30 years), the channel will become empty. The last column of the table shows how many millimetres the sea surface changes per second due to the imbalance. The values that are in the order of 10^{-5} mm/s imply that the sea surface will be changed by 1 mm after about 1 day. We conclude that the volume balances quite perfectly in Channel1, given that we are using only coarse time and spatial resolutions. Now, we perform the same comparison in Crowther Channel.

Another important feature of the flow is that when frictional coefficient is small, the net volume flux is negative (net flow from the east to the west), while the volume flux becomes positive (from west to east) as we increase the frictional coefficient. This result implies the combination of the pressure gradient force and the friction drives the net volume flux to go from the east to west under small frictional coefficient; while the frictional coefficient gets bigger, the combined force drives the net volume flux to go from the west to the east.

run	C_d	$\overline{Q}_{west}$	$\overline{Q}_{east}$	$\Delta\overline{Q}$	$\frac{\Delta V}{\Delta T}$	Q_{ib}	$\frac{Q_{ib}}{V_{total}}$	$\frac{Q_{ib}}{S}$
		$10^3[m^3/s]$	$10^3[m^3/s]$	$[m^3/s]$	$[m^3/s]$	$[m^3/s]$	$10^{-9}/s$	$[10^{-5}mm/s]$
r_4	0.0025	−4.4214	−4.4188	−2.66	0.13	−2.5	−2.0	−6.1
r_5	0.0100	1.6161	1.6165	−0.42	0.02	−0.4	−0.3	−0.9
r_6	0.1000	3.1802	3.1807	−0.47	0.02	−0.5	−0.4	−1.1

Table 5.3: Volume Budget from T_{west} to T_{east} in Channel1 Model Simulations.

5.2.2 Volume Conservation in Crowther Channel

Similarly, we calculate the volume budget in the Crowther Channel from T_{west} to T_{east} (Fig. 5.1 shows their locations), and the controlled domain contains 12,998 triangles with the total area $4.58 \cdot 10^6$ m^2.

run	$\overline{Q}_{west}$	$\overline{Q}_{east}$	$\Delta\overline{Q}$	$\frac{\Delta V}{\Delta T}$	Q_{ib}	$\frac{Q_{ib}}{V_{total}}$	$\frac{V_{ib}}{S}$
	$[m^3/s]$	$[m^3/s]$	$[m^3/s]$	$[m^3/s]$	$[m^3/s]$	$10^{-11}/s$	$[10^{-7}mm/s]$
r_{20}	-7.1114	-7.1376	-0.0261	-0.002	-0.028	-2.4	-4.6
r_{21}	-51.5627	-53.2487	-1.6860	0.000	-1.686	0.3	0.5
r_{23}	10.8091	7.7196	-3.0895	-0.002	-3.092	-2.5	-2.4

Table 5.4: Volume Budget from T_{west} to T_{east} (see Fig. 5.1 for T_{west} and T_{east}'s locations) of Kyuquot Sound Simulations. The differences among the runs are in the parameterization of the horizontal eddy viscosity terms, which are summarized in Table 5.2.

Like what we have seen in Channel1, the volumes are not perfectly balanced in Crowther Channel. But the last two columns of the table suggest that the discrepancy is small enough for us to determine the volume is conserved in Crowther Channel. It takes 3000 years to drain the channel, and about 115 days to have a 1 mm change for the surface, if the same imbalance persists. So this volume balance is actually better than in the simple channel in terms of the ratios, probably due to smaller net volume flux in the Crowther Channel as compared to Channel1. Nevertheless, the balance is good enough for us to proceed.

Now that we have established the volume conservation in Channel1 and in Crowther Channel, we can move forward to energy conservation.

5.3 Energy Conservation

Tidal energy conservation and dissipation have been well studied over the years in both open oceans and estuary locations. de Young and Pond (1987) pointed out three major sinks for barotropic tidal energy: the internal tide, high-frequency internal waves, and friction. Munk (1998) discussed global M_2 tidal dissipation and analyzed different dissipators. Globally, the M_2 tidal dissipation is about 2.5 TW. Despite the difficulties in estimating tidal dissipation in open oceans, Jeffreys (1920), Miller (1966), Cartwright et al. (1980), and Kantha et al. (1995) made estimates on

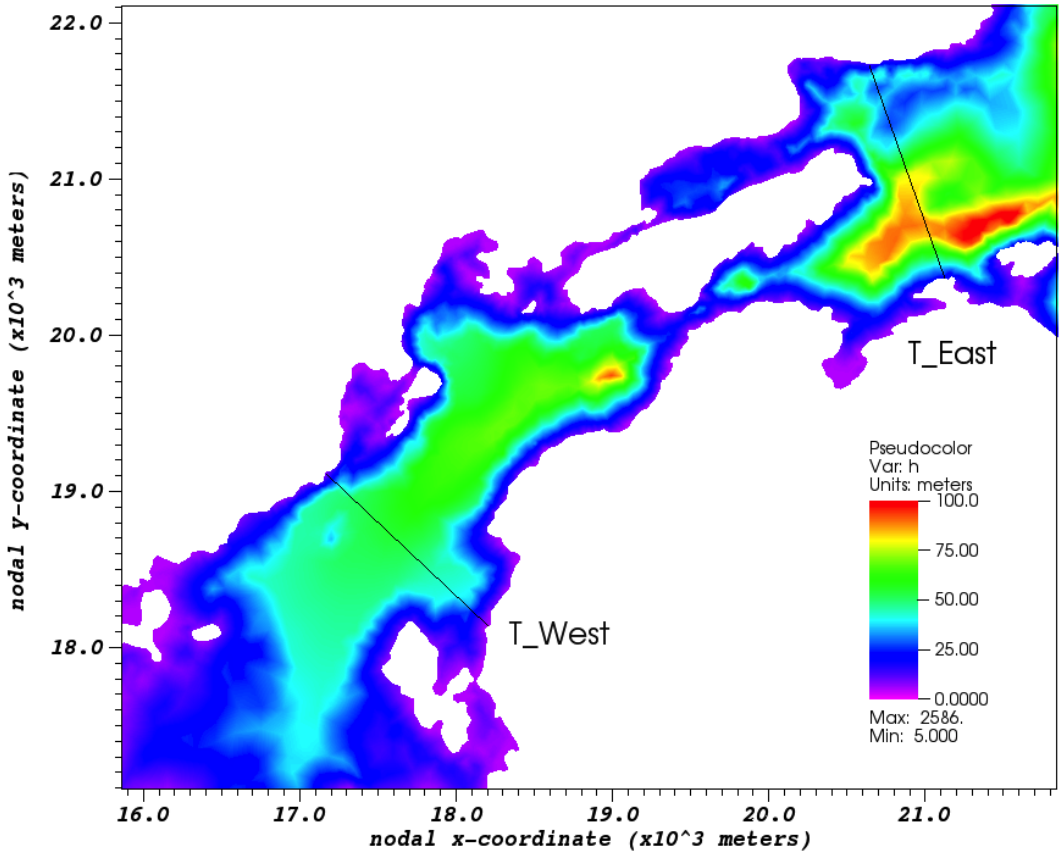

Figure 5.1: Transect T_{west} and T_{east} Locations Overlaid over the Bathymetry Contour

dissipations in Bering Sea, Yellow Sea, European Shelf, Patagonian Shelf, respectively. Energy balances are easier to calculate in confined coastal areas like fjords (Klymak and Gregg, 2004). Greenberg (1979) estimated 20 GW dissipation in the Bay of Fundy, Foreman et al. (1995) estimated 3.3 GW M_2 dissipation in the Salish Sea, and Freeland and Farmer (1980) suggested 10 MW in June and 5 MW in January tidal dissipation in Knight Inlet (a 5 MW seasonal variation).

The energy conservation has also been studied extensively for numerical models as well. As what Ferziger and Peric (2002) pointed out in their book *Computational Methods for Fluid Dynamics*, if a numerical model is energy conserving, and no energy flux enters the system through the free surface, the total energy in the system does not grow in time. This is an important property for numerical models to obtain numerical stability. It does not guarantee the accuracy of the numerical results, but it is still an important property for numerical ocean models, especially for modelling

turbulent and unsteady flows (Marsaleix et al., 2008).

In this section, we first formulate energy conservation equations from the governing equations, then look at the energy conservation of FVCOM by examining the energy budget both in the simple rectangular channel and in Crowther Channel. Secondly, we calculate the predicted energy loss according to the simplified analytical model that we presented in the last chapter; and lastly, we compare these results.

In this section, we use F for the across-channel area integrated energy flux in the unit of W, F_λ for the depth integrated energy flux in W/m, and F_α for the energy flux in W/m^2.

5.3.1 Energy Flux Equations in σ-Coordinates

Here, we formulate the energy equation from the primitive equations that FVCOM uses with salinity, temperature, and density fields turned off. We can re-express the primitive equations in σ-coordinates as [Blumberg and Mellor (1987), Mellor (2004), Chen et al. (2003)]:

$$\frac{\partial(uh)}{\partial t}+\frac{\partial(u^2h)}{\partial x}+\frac{\partial(uvh)}{\partial y}+\frac{\partial(u\omega)}{\partial \sigma}-fvh+gh\frac{\partial \eta}{\partial x}=h(\mathcal{D}_x+\mathcal{F}_x) \tag{5.20}$$

$$\frac{\partial(vh)}{\partial t}+\frac{\partial(uvh)}{\partial x}+\frac{\partial(v^2h)}{\partial y}+\frac{\partial(v\omega)}{\partial \sigma}+fuh+gh\frac{\partial \eta}{\partial y}=h(\mathcal{D}_y+\mathcal{F}_y) \tag{5.21}$$

$$\frac{\partial \eta}{\partial t}+\frac{\partial(uh)}{\partial x}+\frac{\partial(vh)}{\partial y}+\frac{\partial \omega}{\partial \sigma}=0 \tag{5.22}$$

where ω is the cross-sigma-coordinate velocity, and the vertical $[\mathcal{D}=(\mathcal{D}_x,\mathcal{D}_y)]$ dissipative terms are:

$$(\mathcal{D}_x,\mathcal{D}_y)=\left[\frac{1}{h}\frac{\partial}{\partial \sigma}\left(\frac{K_m}{h}\frac{\partial u}{\partial \sigma}\right),\frac{1}{h}\frac{\partial}{\partial \sigma}\left(\frac{K_m}{h}\frac{\partial v}{\partial \sigma}\right)\right] \tag{5.23}$$

and the horizontal $[\mathcal{F}=(\mathcal{F}_x,\mathcal{F}_y)]$ dissipative terms are shown in Eqns. 5.4.

Define the σ average of any function ψ as:

$$\overline{\psi}=\int_{-1}^{0}\psi d\sigma \tag{5.24}$$

Following Kelly et al. (2010) velocity decomposition, and defining the depth-averaged velocity as the barotropic velocity:

$$\overline{\mathbf{u}} = \int_{-1}^{0} \mathbf{u} d\sigma, \tag{5.25}$$

we have the velocity decomposition:

$$\mathbf{u} = \overline{\mathbf{u}} + \tilde{\mathbf{u}} \tag{5.26}$$

where $\tilde{\mathbf{u}}$ is the perturbation from the vertically averaged component. Note that even though we do not have density and salinity fields, the viscosity terms still cause the velocity to have vertical perturbations so this decomposition is not trivial (i.e. $\tilde{\mathbf{u}}$ is not necessarily zero). In addition, currents over varying topography drive vertical velocities. A first-order approximation is that they currents mostly follow the sigma surfaces but it is not guaranteed. Given the definition of $\overline{u}$, we have:

$$\int_{-1}^{0} \tilde{\mathbf{u}} d\sigma = 0 \tag{5.27}$$

Following Carter et al. (2008), the σ-averaged momentum equations can be written as:

$$\frac{\partial \overline{u}}{\partial t} + \overline{\mathcal{A}'_x} - f\overline{v} + g\frac{\partial \eta}{\partial x} = \overline{\mathcal{D}_x} + \overline{\mathcal{F}_x} \tag{5.28}$$

$$\frac{\partial \overline{v}}{\partial t} + \overline{\mathcal{A}'_y} + f\overline{u} + g\frac{\partial \eta}{\partial y} = \overline{\mathcal{D}_y} + \overline{\mathcal{F}_y} \tag{5.29}$$

where

$$\overline{\mathcal{A}'_x} = \overline{u}\frac{\partial \overline{u}}{\partial x} + \overline{v}\frac{\partial \overline{u}}{\partial y} + \frac{1}{h}\left\{\frac{\partial}{\partial x}\left[h\left(\overline{u^2} - \overline{u}^2\right)\right] + \frac{\partial}{\partial y}\left[h\left(\overline{uv} - \overline{u}\ \overline{v}\right)\right]\right\} \tag{5.30}$$

$$\overline{\mathcal{A}'_y} = \overline{u}\frac{\partial \overline{v}}{\partial x} + \overline{v}\frac{\partial \overline{v}}{\partial y} + \frac{1}{h}\left\{\frac{\partial}{\partial x}\left[h\left(\overline{uv} - \overline{u}\ \overline{v}\right)\right] + \frac{\partial}{\partial y}\left[h\left(\overline{v^2} - \overline{v}^2\right)\right]\right\}, \tag{5.31}$$

and we have the approximations by Chen et al. (2003) in FVCOM

$$\overline{\mathcal{F}_x} \approx 2 \cdot \frac{1}{h}\left\{\frac{\partial}{\partial x}\left(\overline{2A_m H\frac{\partial u}{\partial x}}\right)+\frac{\partial}{\partial y}\left[\overline{A_m H\left(\frac{\partial u}{\partial y}+\frac{\partial v}{\partial x}\right)}\right]\right\}- \frac{1}{h}\left\{\frac{\partial}{\partial x}\left(2\overline{A_m}H\frac{\partial \overline{u}}{\partial x}\right)+\frac{\partial}{\partial y}\left[\overline{A_m}H\left(\frac{\partial \overline{u}}{\partial y}+\frac{\partial \overline{v}}{\partial x}\right)\right]\right\} \tag{5.32}$$

$$\overline{\mathcal{F}_y} \approx 2 \cdot \frac{1}{h}\left\{\frac{\partial}{\partial x}\left[\overline{A_m H\left(\frac{\partial u}{\partial y}+\frac{\partial v}{\partial x}\right)}\right]+\frac{\partial}{\partial y}\left(\overline{2A_m H\frac{\partial v}{\partial y}}\right)\right\}- \frac{1}{h}\left\{\frac{\partial}{\partial x}\left[\overline{A_m}H\left(\frac{\partial \overline{u}}{\partial y}+\frac{\partial \overline{v}}{\partial x}\right)\right]+\frac{\partial}{\partial y}\left(2\overline{A_m}H\frac{\partial \overline{v}}{\partial y}\right)\right\}. \tag{5.33}$$

The dissipation due to vertical eddy viscosity can also be evaluated, given that the surface stress is 0 [Chen et al. (2011)]:

$$\overline{\mathcal{D}_x} = \int_{-1}^{0}\frac{1}{h}\frac{\partial}{\partial\sigma}\left(\frac{K_m}{h}\frac{\partial u}{\partial\sigma}\right)d\sigma = -\frac{1}{h}C_d u_b\sqrt{u_b^2+v_b^2} \tag{5.34}$$

$$\overline{\mathcal{D}_y} = \int_{-1}^{0}\frac{1}{h}\frac{\partial}{\partial\sigma}\left(\frac{K_m}{h}\frac{\partial v}{\partial\sigma}\right)d\sigma = -\frac{1}{h}C_d v_b\sqrt{u_b^2+v_b^2}. \tag{5.35}$$

Now combining the σ-averaged continuity equation:

$$\frac{\partial\eta}{\partial t}+\frac{\partial\overline{u}h}{\partial x}+\frac{\partial\overline{v}h}{\partial y}=0 \tag{5.36}$$

we obtain the σ-averaged barotropic energy density equation by adding these three terms together:

$$h\overline{u}(5.28)+h\overline{v}(5.29)+(g\eta)(5.36). \tag{5.37}$$

Note that this energy formulation only considers the barotropic energy (energy calculated from the vertically averaged velocity). In Carter et al. (2008)'s paper, the energy loss from the barotropic part provides the energy source in the baroclinic energy balance. In our case, we compare the vertically averaged velocity and the velocity field deviated from the vertical average by integrating $\overline{\mathbf{u}}^2$ and $\tilde{\mathbf{u}}^2$ over the channel domain from T_{west} to T_{east}, and averaging over one tidal cycle (see Table 5.5). These quantities (i.e. can be viewed as energy density) provide good estimations on the relative

importance of the non-depth averaged in each of the three runs. The results indicate that (1) for all three runs, the energy densities derived from the non-depth averaged velocities are significantly smaller than the barotropic energy density component (5 and 9 orders of magnitude smaller), and (2) the energy densities derived from the non-depth averaged velocities become more significant when we use Smagorinsky turbulence closure scheme for medium and low eddy viscosity coefficients (r_{21} and r_{23}). We will discuss the possible complications further in both section 5.4 and the conclusion chapter. But here, we assume that the energy sink from the barotropic (depth averaged) energy balance to non-depth averaged energy balance is 0 (i.e. the conversion is 0).

runs	Constant A_m [m^2/s]	Smagorinsky C	$\int \overline{u}^2 dv$ $10^9 m^5/s^2$	$\int \overline{v}^2 dv$ $10^9 m^5/s^2$	$\int \tilde{u}^2 dv$ m^5/s^2	$\int \tilde{v}^2 dv$ m^5/s^2
r_{20}	20.0		0.36	0.24	2.60	0.82
r_{21}		5.0	4.11	2.20	$1.70 \cdot 10^4$	$7.08 \cdot 10^3$
r_{23}		1.0	7.56	3.93	$3.33 \cdot 10^4$	$1.80 \cdot 10^4$

Table 5.5: Comparisons between $\int \overline{\mathbf{u}}^2 dv$ and $\int \tilde{\mathbf{u}}^2 dv$.

Following Carter et al. (2008)'s partitioned energy terminologies, we have the following energy terms in the barotropic energy (m^3/s^3) equation, and write them in separate terms:

$$\begin{aligned}
\text{Tendency } \left(\frac{dE}{\rho dt}\right) &: h\frac{\partial}{\partial t}\left(\frac{\overline{u}^2+\overline{v}^2}{2}\right) + \frac{\partial}{\partial t}\left(g\frac{\eta^2}{2}\right) \\
\nabla\cdot \text{ Flux: } &+ \frac{\partial}{\partial x}\left(h\overline{u}g\eta\right) + \frac{\partial}{\partial y}\left(h\overline{v}g\eta\right) \\
\text{Advection: } &+ h\overline{u}\overline{\mathcal{A}'_x} + h\overline{v}\overline{\mathcal{A}'_y} \\
\text{Conversion: } &= 0 \\
\text{-Explicit Dissipation (-ED): } &+ h\overline{u}\left(\overline{\mathcal{D}_x} + \overline{\mathcal{F}_x}\right) + h\overline{v}\left(\overline{\mathcal{D}_y} + \overline{\mathcal{F}_y}\right)
\end{aligned} \tag{5.38}$$

Note that in our context the term barotropic means the vertically-averaged quantity, and the rest is the deviation from the vertically-averaged quantity [see Carter et al. (2008) for more details]. Also, we are defining the combination of the vertical dissipation and the horizontal dissipation as the explicit dissipation (ED), which is all the dissipation that we can account for. The negative sign in front of ED is to make

sure the dissipation terms are positive, providing that the vertical dissipation (VD) is: $-\left[h\overline{u}(\overline{\mathcal{D}_x}) + h\overline{v}(\overline{\mathcal{D}_y})\right]$, and the horizontal dissipation (HD) is: $-\left[h\overline{u}(\overline{\mathcal{F}_x}) + h\overline{v}(\overline{\mathcal{F}_y})\right]$.

Eqn. 5.38 is the energy flux density equation ($\mathrm{W/m^2}$). Integrating the equation over area of a channel section and multiplying by density, we will get the energy equation in kg $\mathrm{m^2/s^3}$ (Joule), and an energy balance should hold:

$$\int \frac{dE}{dt} dA + \int \nabla \cdot \mathrm{F}_\lambda dA + \int \text{Advection } dA + \text{VD} + \text{HD} = 0 \tag{5.39}$$

If we apply the divergence theorem to the divergence of flux term (the second term on the left hand side), we only need to calculate the flux going through the boundaries of the channel section, given that we have zero net energy flux at the sea surface and crossing normal to closed land boundaries (a few tests have been performed to confirm the energy flux across closed land boundaries are small enough to be ignored):

$$\int \nabla \cdot \mathrm{F}_\lambda \, dA = \oint F_\lambda \cdot dl \tag{5.40}$$

$$= F_{east} - F_{west} \tag{5.41}$$

where F_{west} and F_{east} denote the energy flux at the west and the east transect, respectively. Next, we will show the energy balance results of the rectangular Channel and Crowther Channel.

5.3.2 Energy Budget in the Rectangular Channel

All terms in the energy equation are calculated for 3 runs (r_4, r_5 and r_6, see Table 5.1 for their differences) in the rectangular channel, and the results are shown in Table 5.6.

There are two balances that we list in the table Imbalance1 and Imbalance2 - numerical integrated energy balance residual terms, and they are defined as:

$$\text{Imbalance1} = \int \frac{dE}{dt} dA + \int \nabla \cdot F_\lambda dA + \int \text{Advection } dA + \text{VD} + \text{HD} \tag{5.42}$$

$$\text{Imbalance2} = \int \frac{dE}{dt} dA + \oint F_\lambda \cdot dl + \int \text{Advection } dA + \text{VD} + \text{HD} \tag{5.43}$$

The differences between these two are the ways that we calculate the energy flux term

in the energy equation. In imbalance2, we have applied the Stokes' Theorem, and obtained the energy flux term by calculating the difference in energy flux at the two open boundaries; while in imbalance1, we sum over the $\nabla \cdot F$ term over the entire domain. Two methods are used here so that we have a better understanding of how much the results could be affected by our choice of the numerical methods.

	r_4	r_5	r_6
C_d	0.0025	0.0100	0.1000
Energy Term	$[KW]$	$[KW]$	$[KW]$
dE/dt	-0.001	-0.001	-0.002
F_{west}	-240043.539	-232500.093	-229654.384
F_{east}	-241404.949	-233315.521	-229926.066
Δ F =F_{east} - F_{west}	-1361.410	-815.428	-271.682
$\sum \nabla \cdot$ F	-1345.220	-790.573	-262.011
Advection	-18.869	1.851	-5.171
Ver D	1319.130	832.945	315.199
Hor D	0.134	0.000	0.000
Imbalance1	-61.02	19.337	38.145
Imbalance1/ ED (%)	-4.62%	2.32%	12.10%
Imbalance2	-44.83	44.221	48.014
Imbalance2 /ED (%)	-3.40%	5.31%	15.23%
Δ F / Flux_Ave Flux_Ave = 0.5$\cdot$ (F_{west} +F_{west})	0.57%	0.35%	0.12%

Table 5.6: Channel 1 r_4, r_5, and r_6 Energy Budget Results Summary - T_{west} to T_{east}. ED is the explicit dissipation (vertically dissipation and the horizontal dissipation).

A good agreement of the energy balance (Table 5.6) is reached (less than 5% of imbalance for r_4 and r_5). While the balance for r_6 is not as good, the flux difference between two transects for r_6 is a small percentage (0.12%) of the average flux (the last row of Table 5.6 shows the resolution that we need to resolve in terms of the percentage of averaged the energy flux). It is possible that the interpretation methods that we used here is not good enough to resolve better than 90% energy balance when we look at a 0.12% in the total energy loss, however, further studies are needed to understand this imbalance.

There are a few other observations that we would like to note from the energy budget calculation.

- The stability terms (dE/dt) from all three runs are small, suggesting the simulation has reached a steady state during the cycle the we are analyzing.
- As the frictional coefficient increases (r_4 has the smallest frictional coefficient, and r_6 has the biggest one), the difference of the energy flux between the west transect (T_{west}) and the east transect (T_{east}) decreases. This indicates that when we increase the frictional coefficients, the energy loss actually decreases due to decreased velocity, and the total energy flux decreases as well while we increase the frictional coefficients.
- As the frictional coefficient increases, the vertical dissipation term decreases due to decreased velocity.
- Two methods of calculating the energy flux give close results [$O(1\%)$, not statistically significant], suggesting that the discretized divergence theorem implemented here is a good way to calculate net energy flux. In fact, the discretized divergence theorem (calculating the net flux as the boundary difference instead of summing) should be a better way of evaluating the net energy flux, especially when the flow is more turbulent. Because calculations of the divergence of the flux uses first order least-squared linear approximations (see Appendix A.1), the summing process could potentially accumulate more errors.

Now, let us move on to the Energy budget in Crowther Channel.

5.3.3 Energy Budget in Crowther Channel

Energy terms are calculated for 3 of the Kyuquot runs (r_{20}, r_{21}, and r_{23}). The differences among three runs are in the parameterizations of the horizontal eddy viscosity (see Table 5.2). Discrete divergence theorem (energy flux term is calculated as the net flux from two open boundaries) is used to calculate the net energy flux to minimize numerical approximation errors because the flow is more turbulent in Crowther Channel. We examine the following energy imbalance:

$$\text{Imbalance} = \int \frac{dE}{dt} dA + \oint F_\lambda \cdot dl + \int \text{Advection } dA + \text{VD} + \text{HD}. \tag{5.44}$$

As what we have expected, the energy balances (see Table 5.7) are worse for all three runs, as compared to in Channel1. A good balance is achieved for r_{20} and r_{21}

(about 85%), while a 90% discrepancy (relative to the explicit dissipation) is seen for r_{23} when the horizontal dissipation coefficient (C) is small in Smagorinsky turbulent closure scheme. The larger discrepancy in r_{23} along with a more thorough analysis is discussed in the Discussion section later in this chapter.

The energy fluxes in all three runs are negative at both west and east transects, implying that the energy flows into the channel from the east end and loses energy as it travels to the west end (the magnitude of the energy flux on the west end is smaller than at the east end for all three runs). This result seems surprising but is interesting. The energy is actually forced by the Kyuquot Channel, flowing from the east to the west into the open ocean. In fact, this energy is driven by the the elevations at the two ends of Crowther Channel. We have demonstrated earlier that the phase of the elevation is almost the same everywhere in Kyuquot Sound. However, the elevation amplitude in Kyuquot Channel is slightly bigger than the one at the open ocean end of the Crowther Channel (see Fig. 5.2). Given that the phases in Kyuquot Sound is constant, this amplitude difference is responsible for the westward energy flux.

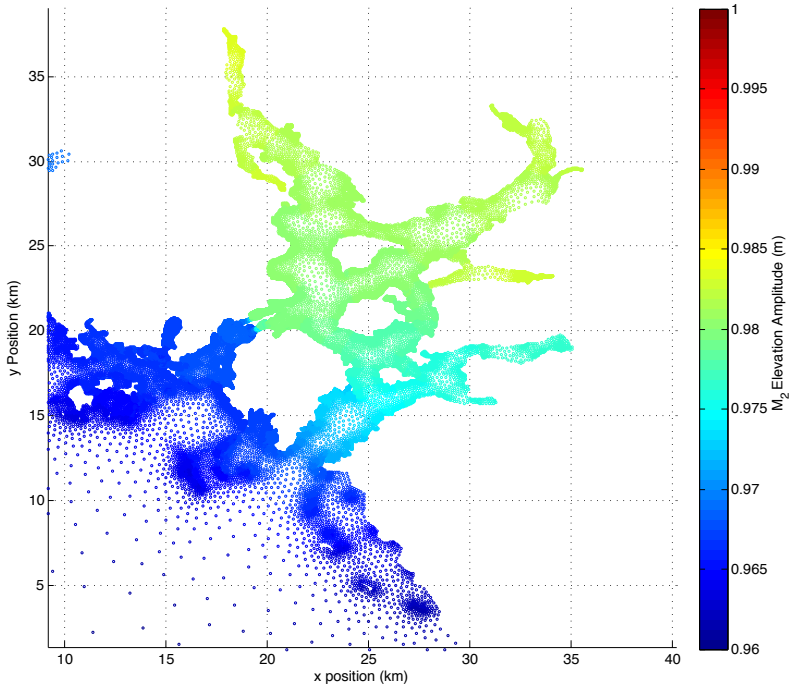

Figure 5.2: Sea Surface Elevation M_2 Amplitude in Kyuquot Sound.

Among these three runs, r_{20} has the largest horizontal eddy viscosity coefficient (A_m is 20 m^2/s everywhere). In r_{21}, the largest A_m in the Crowther Channel is about 8 m^2/s, and it is even smaller for r_{23}. As we decrease the horizontal eddy viscosity

coefficient(A_m): (1) the flux going into the channel increases (magnitude of F_{west} and F_{east}) because we have increased velocity in the entire domain (Table 5.2 gives an idea about the velocity in the channel. The velocity at T_{west} increases from r_{20} to r_{23}); (2) the advection term increases because non-linear processes are not damped out as much by horizontal viscosity, and become more important; (3) the horizontal dissipation term does not vary accordingly because it is affected by a combination of both the current velocity and the eddy coefficient; (4) the imbalance increases. The reasons could be many and we will discuss them in the section 5.4.

	r_{20}	r_{21}	r_{23}
Term	$[KW]$	$[KW]$	$[KW]$
dE/dt	-0.000	-0.038	0.000
F_{west}	-857.564	-3828.620	-4524.798
F_{east}	-866.983	-3871.851	-4583.148
Δ F=F_{east} - F_{west}	-9.419	-43.231	-58.418
Advection	-0.001	4.037	9.122
Ver Dissipation	0.014	0.370	0.627
Hor Dissipation	11.096	45.819	24.659
Imbalance	-1.67	6.939	-22.87
Imbalance/ ED (%)	-15.03%	15.02%	90.45%

Table 5.7: r_{20}, r_{21}, and r_{23} Results Summary - T_{west} to T_{east}.

Next, we look at the energy balance calculated from the simplified analytical model.

5.3.4 Energy Balance in the Side Channel of the Simplified Analytical Model

In the previous chapter, we presented a simplified analytical model to represent the circulation in a two-channel system. The change in the phase difference between the velocity and the sea surface elevation along the channel suggests that energy is lost in the side channel when we have a non-zero friction coefficient.

The energy flux difference between a west and an east transect (point in this case) should be balanced by what is lost to friction, assuming that we are at steady state ($\frac{\partial E}{\partial t} = 0$):

$$\Delta F_\lambda = \rho \int r_1 \overline{u_1 \cdot u_1} dl, \tag{5.45}$$

where ρ is the water density, u_1 is the tidal current velocity, and ΔF is the energy flux difference between two points. F at any point is evaluated as (Garrett, 1975):

$$F_\lambda = \rho g h \overline{u_1 \eta_1}, \tag{5.46}$$

where the overbar denotes the time average.

The trapezoidal rule is used to evaluate the time average, providing $dt = 12.42s$, $\rho = 1025$ kg/m^3, $g = 9.81$ m/s^2, $h = 30$ m, $r = r_1 = 0.007$ m/s , and the positive direction is defined from the west to east.

Let us use the T_{west} and T_{east} locations as our reference point from the Crowther Channel. They are approximately at $x = 2600$ m and $x = 6600$ m, respectively. Then the power flux per unit length at these two locations of the side channel are computed:

$$F_{\lambda west}(x = 2600) = -2.5389 \cdot 10^3 \text{ W/m} \tag{5.47}$$

$$F_{\lambda east}(x = 6600) = -2.5448 \cdot 10^4 \text{ W/m}. \tag{5.48}$$

Negative power flux means the energy flow direction is from the east to the west end. Some energy is lost when going through the side channel. The energy removed ($F_{\lambda west} - F_{\lambda east} = 5.8775$ W/m) from the frictional process per unit area in the side channel can be calculated by dividing the difference of the two energy flux by the total length ($L = 4000$ m):

$$F_\alpha = (F_{east} - F_{west})/L \tag{5.49}$$

$$= 1.469 \cdot 10^{-3} \text{ W/m}^2 \tag{5.50}$$

This energy loss should be balanced by the friction dissipation per unit area (F'_α) at the bottom in the side channel:

$$F'_\alpha = \rho \int r_1 \overline{u_1 \cdot u_1} dl/L$$
$$= 1.471 \cdot 10^{-3} \text{ W/m}^2 \tag{5.51}$$

F_α and F'_α are consistent up to 0.1%. This suggests that the energy dissipated by the bottom frictional process almost exactly balances the energy flux difference calculated from the western and the eastern ends of the side channel.

The distribution of the energy flux along the side channel is shown in Fig. 5.3. The energy is monotonically decreasing as the it goes from the east to the west, and the negative overall energy flux suggests that the energy is coming from the east end of the channel.

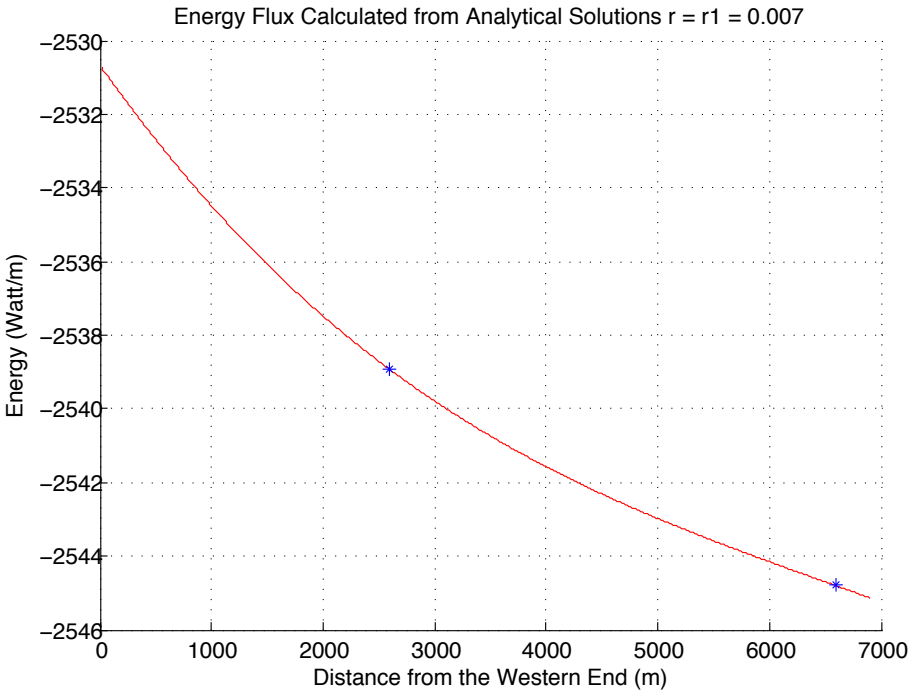

Figure 5.3: Energy Flux Calculated from Analytical Solutions Along the Side Channel (using fitted $r = r_1 = 0.007$ obtained from the previous chapter for illustration). The left and the right asterisks are the approximate locations of T_{west} and T_{east}, respectively.

The behaviour of the side channel energy flux changes when different friction coefficient (r_1) is applied (see Fig. 5.4). As r and r_1 increase, the magnitude of the negative net energy flux decreases. Eventually for r_{23}, the energy flux at the western

end becomes positive. This implies that when the friction is large, energy is coming into the channel from both ends and get dissipated in the interior of the channel.

A comparison between the energy calculated from the FVCOM model results and from the simplified analytical model is a part of the following section.

5.4 Discussion

In this section, we discuss the energy balance (imbalance) and connections between the analytical model and the numerical results.

5.4.1 Energy from Numerical Results

The kinetic energy equation is a consequence of the momentum equations, so the discretized kinetic energy equation should be a consequence of the discretized momentum equations in numerical methods. Because the kinetic energy equation and the momentum equation are not independently formed, it is not possible to exactly enforce the kinetic energy equation, while enforcing the momentum equation in a finite-volume numerical method (Ferziger and Peric, 2002). There are a few reasons that can explain the imperfection of the energy balance, and here are the major ones:

- **Energy Equation Formulation**: When following Carter et al. (2008)'s energy formulation, we only considered the σ-averaged energy balance assuming that energy component deviated from the σ-averaged energy is small enough to be ignored. This assumption is valid when the σ-averaged component dominates the process and it is the case for the simple rectangular Channel1 where the energy balances almost exactly. In Kyuquot Sound runs where we have more complex coastal lines and topography, the energy balance is about 85% for two runs (r_{20} and r_{21}), but the imbalance is almost the same as the explicit dissipation in magnitude for the more turbulent run (r_{23}). It might be necessary to re-formulate the energy in a different way in order to capture the total energy. This is discussed and emphasized further in the conclusion chapter.

- **Horizontal Mixing**: In the Smagorinsky turbulent closure scheme, because all horizontal mixing is assumed to only occur along sigma levels. As a consequence, the dissipation calculated from the horizontal viscosity term has a vertical mixing component [Marsaleix et al. (2008), Chen et al. (2003)]. The

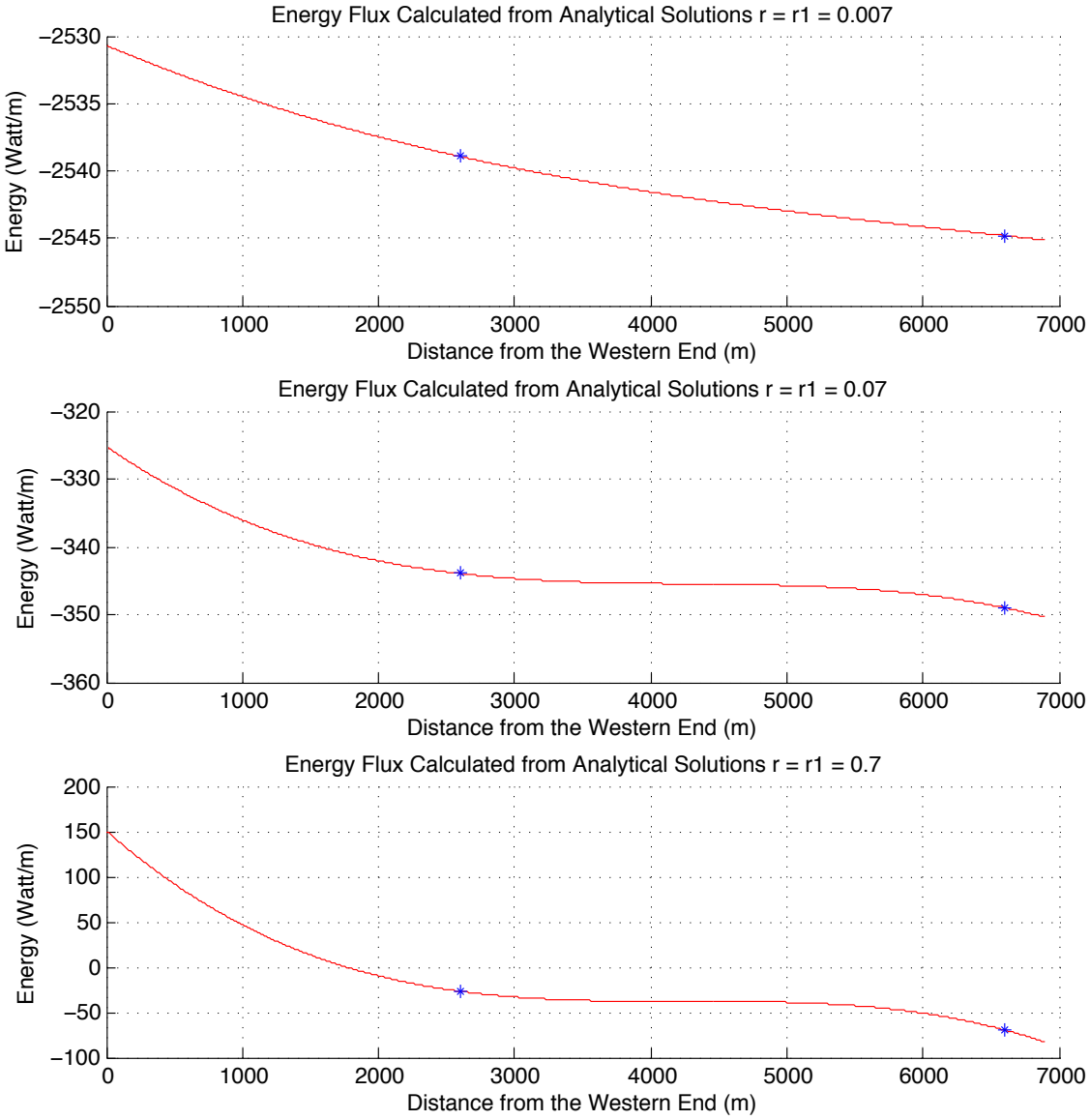

Figure 5.4: Energy Flux of the Side Channel with Different $r1$ Coefficients. The left and the right asterisks are the approximate locations of T_{west} and T_{east}, respectively.

diffusivity parameterization (Mellor and Blumberg, 1985) provides a more accurate way to approximate the horizontal eddy diffusion term in σ-coordinates. However, this approach essentially assumed the horizontal diffusion occurs only parallel to the σ-layers, which induces extra vertical diffusion terms, and this might imply larger non-σ-averaged energy component.

- **Internal and External Mode**: FVCOM implements a 'mode splitting' numerical method that divides the currents into external and internal modes, and computes the solutions separately in both modes. Chen et al. (2003) and Blumberg and Mellor (1987) provided more details. As a result, there exists disagreement between the forcing terms (solved under internal mode) and the velocities (adjusted in every internal step according to the external mode results). This could result an inaccuracy in the energy.

- **Interpolations**: In FVCOM, vector variables (such as u and v) are located at the centres of the triangles, while scalar variables (such as η and h) are located at the nodes of the triangles. Linear least-square interpolation method is used to obtain all needed variables onto the same location (on transect lines for energy flux, and centres of triangles for other quantities) in order to calculate each of the energy terms (Appendix A gives detailed steps of interpolations) . The linear interpolation could potentially be a large contributor to the imbalance, especially when the the flow is more turbulent (e.g. r_{23}).

Despite all the potential reasons that could cause the energy balance imperfection, it is still interesting to check how well the energy balances when we take time averages over a longer period. In the previous sections, the last simulation cycle has been used because we have been assuming the last cycle (Cycle 20) should be the closest to the steady state. But as what Marsaleix et al. (2008) suggested, some of the errors are likely to be smaller if we take a longer period. Now, we look at the energy balance for all three Kyuquot runs over the last 15 cycles.

Previously, during the volume and energy conservation tests, r_{23} gives poorer balance as compared to r_{20} and r_{21}. Now, we calculate the energy flux at T_{west} and T_{east}, and their differences (see Fig. 5.5). After the 10^{th} cycle, both r_{20} and r_{21} reach a steady state in energy, while the imbalance is still scattered for r_{23}.

Another way to look at the balance is to average the energy budget over a number of cycles. It is clear that the imbalance does not vary much when averaging over a

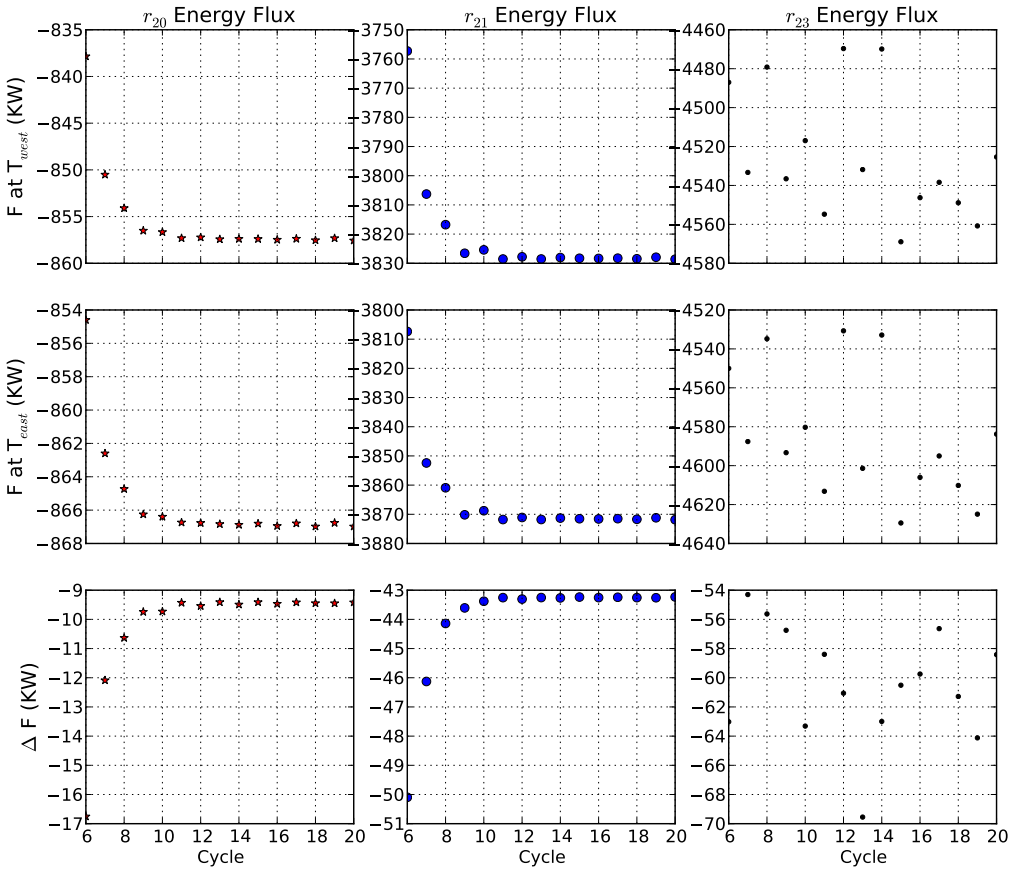

Figure 5.5: Energy flux at T_{west} and T_{east} from three Kyuquot runs (r_{20}, r_{21} and r_{23}). The first row is the energy flux at the west transect, the second row is the east transect, and the third row is the difference between the two.

number of cycles for r_{20} and r_{21} (within 1%), but not for r_{23} (see Fig. 5.6). A small $[O(0.1\%)]$ but noticeable 2-cycle oscillation are present in the averaging imbalance for r_{20} and r_{21}, suggesting a better time resolution might be in need to eliminate this oscillation. Nonetheless, this small oscillation does not affect our major concern here. This result further indicates that the method that we are using might not be a good fit for more turbulent flows.

Numerical dissipation is another factor that needs to be discussed here. It has long been recognized that the discrete model might be artificially dispersive, while the governing equations are not. This artificial dispersion is generally called numerical dissipation, numerical diffusion, and it arises from truncation errors, when the explicit dissipation is not large enough to balance the discretized equation. These artificial terms are analogous to a diffusion process, and they can be in the direction normal to the flow or in the streamline direction (Ferziger and Peric, 2002). Numerical diffusion is not avoidable with numerical models, but can be limited by having finer grid and smaller time step.

If we assume the model conserves energy relatively well, this scattered energy flux in r_{23} is likely due to a combinations of the following reasons: (1) the barotropic energy formulation that we adapted from Carter et al. (2008) might not be sufficient enough to capture the energy flux when the flow is more turbulent; (2) the model has not been run long enough to reach a steady solution; (3) the explicit dissipation (vertical + horizontal) is not enough to balance the energy loss, suggesting there is some numerical dissipation that we did not account for. Nevertheless, the scattered energy flux over a number of cycles explains the larger discrepancy of r_{23} in the energy and volume budget.

Despite all the imperfections in the methods and imbalances, fortunately for us, 80% of energy balance (r_{20} and r_{21}) is good enough to allow us to look at the bigger picture that we connect the numerical energy results and the analytical model results.

5.4.2 Analytical Model Results v.s. Numerical Results - The Bigger Picture

The energy flux in Crowther Channel is lost to frictional processes. This energy loss is directly related to the phase difference variation that we have observed in Crowther Channel. By using complex numerical models, such as FVCOM, we can get relatively accurate flow circulation information in the channel. However, these numerical mod-

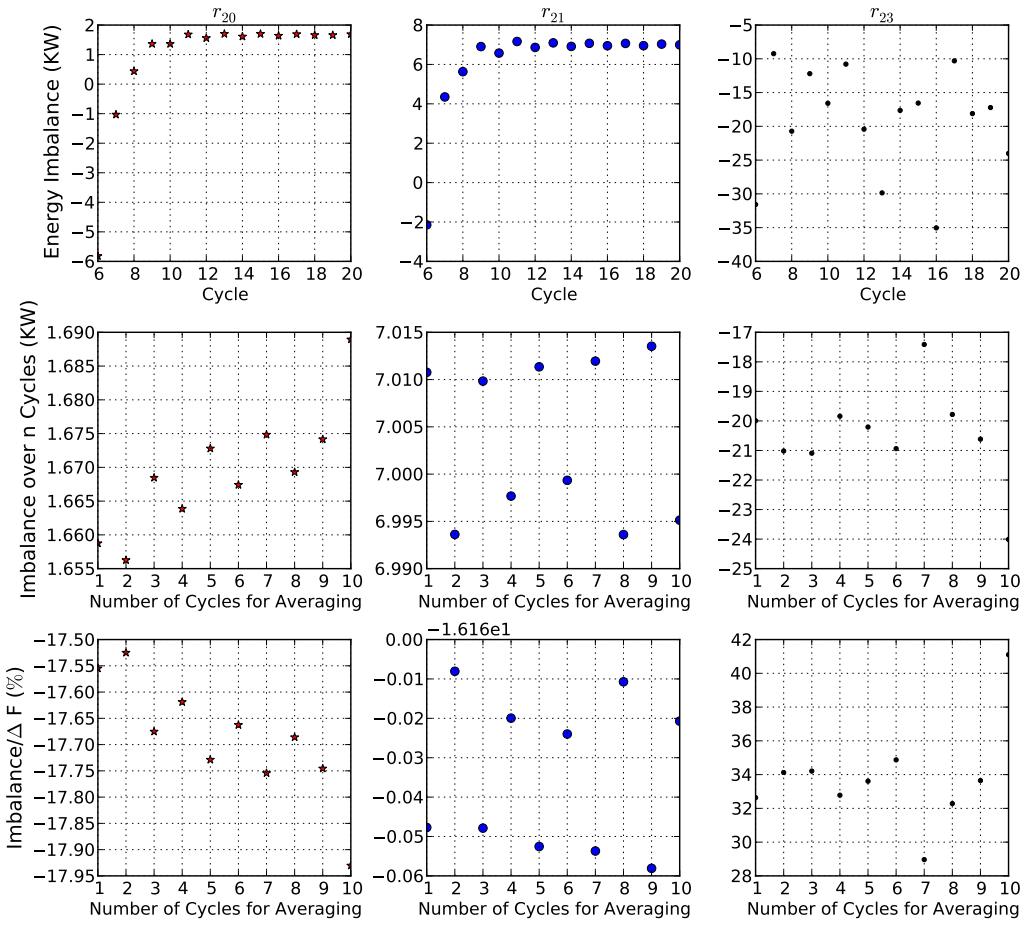

Figure 5.6: Energy flux imbalance between T_{west} and T_{east} from three Kyuquot runs (r_{20}, r_{21} and r_{23}). The first row is the energy imbalance over the last 15 cycles, the second row is the imbalance averaged over a number of cycles, and the third row shows the ratio of the averaged imbalance to the energy flux difference.

els are usually computationally expensive. If provided with two elevation phases at entrances of the dominant channel and the secondary channel and an appropriate frictional coefficient, we can use our analytical model to estimate the energy dissipation in the channel, and to further estimate the current phase in the channel. The bigger question here is how good our analytical model is at estimating energy dissipation in the secondary channel of a two-channel system.

In this section, we compare the energy loss per unit area in the analytical model results and the numerical results to answer the question. For the sake of completeness, we include r_{23} in all our comparisons.

Simplified Analytical Results	r_{20} fit	r_{21} fit	r_{23} fit
r and $r1$	0.007	0.007	0.005
Unit Area Dissipation (W/m^2)	0.0015	0.0012	0.0012
Numerical Runs	r_{20}	r_{21}	r_{23}
Unit Area Dissipation (W/m^2)	0.0020	0.0084	0.0044

Table 5.8: r_{20}, r_{21}, and r_{23} Numerical and Analytical Results Comparison Summary - T_{west} to T_{east}.

First, we find the approximate frictional coefficients for all three runs by fitting the phases along the channel (see Fig. 5.7), and we calculate the energy loss per unit area in W/m^2. Then we calculate the same quantities from the numerical models (see Table5.8). The unit area dissipation of the numerical runs is calculated from dividing the total volume by the averaged depth in the Crowther Channel (30 m), which is also the depth that we assumed in the simple analytical model.

These results show a good agreement in the unit area dissipation for r_{20} (0.0015 v.s. 0.0020 W/m^2). It is not great for r_{21} but the predicted dissipation rate (analytical results) is still in the same order of magnitude as the numerical results. This simple but straightforward result suggests that despite the simplicity of the analytical model, it can provide good estimations of the energy dissipation rate in a channel with a complex bottom topography and coastal lines.

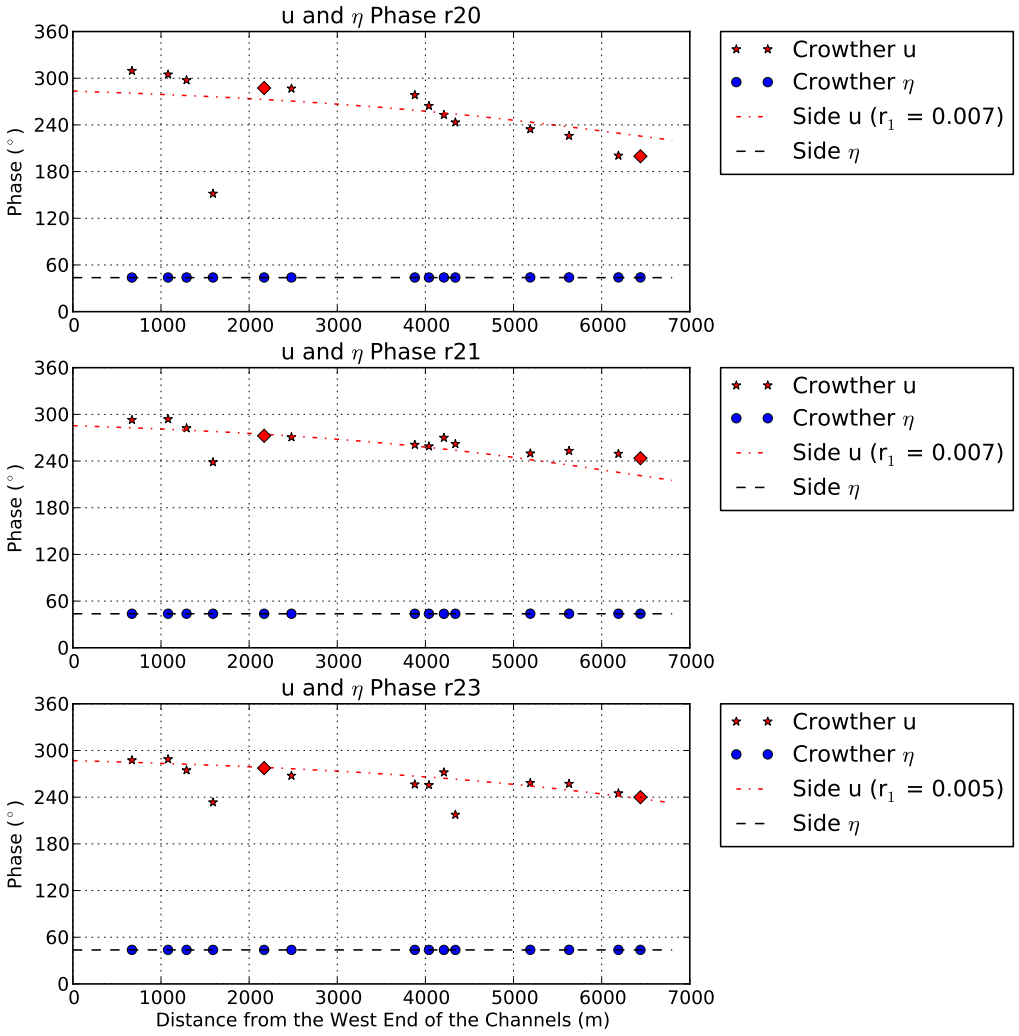

Figure 5.7: Velocity and Sea Surface Elevation Phase Plot from the Side Channel Analytical General Solutions and from 3 model runs.. Red diamonds are the approximate location of the west and east transects that we have been using for analyses.

Chapter 6

Conclusion

6.1 Summary

We examined the barotropic M_2 tidal circulation and associated oceanographic properties in the Kyuquot Sound. Our main findings are:

- **Phase Difference**: We have found that there is an along-channel phase difference variation in Crowther Channel due to the shallow topography in Kyuquot Sound. In Kyuquot Channel (the main channel), the barotropic tidal circulation behaves like a standing wave, having an almost-90° phase difference between currents and elevation. In Crowther Channel, the phase difference between currents and elevation is not 90°, but varies as we move along the channel.

- **Energy Flux Direction**: In Crowther Channel, the net energy flux is flowing from the east end (Kyuquot Channel side) to the west end (open ocean side). The cause is that while the phase of the elevation is constant throughout the sound, the elevation amplitude at the east end is slightly bigger than at the west end. This elevation difference drives the energy in Crowther Channel from the Kyuquot Channel end to the open ocean end.

- **Role of Friction**: In Crowther Channel, friction is responsible for the phase difference that we have observed. In deep inlets, the phase difference between currents and elevation is 90°, while in shallow waters, the phase difference usually varies along channel. The averaged depth in Crowther Channel is much smaller than the one in Kyuquot Channel (30 m v.s. 150 m), and this topographic feature causes the phase difference variation that we see in Crowther

Channel.

- **Simple Analytical Model Estimation**: We have compared the energy dissipation rate per unit area due to friction between the simple analytical model and the fully non-linear numerical model (FVCOM). These results are consistent except in cases when the flow is more turbulent, where we suspect that the numerical dissipation may be responsible for the imbalance. This consistency corroborates the simplified assumptions of physics in the simplified analytical model, providing a simple tool to describe the circulation in a two-channel system.

We have also focused on the volume and energy balance in FVCOM. While the volume balance is good in the test channel (Channel1) and Crowther channel, there are several changes that could have been made to improve the FVCOM energy balance investigations presented here. We list some of the major ones:

- **Run Energy Balance Calculation Online**: The time step of the stored numerical results that we use is 10^5 times more than the time step that the model actually uses. If time and resource permits, we could run a diagnostic analysis inside FVCOM to compute energy online. This would eliminate any problems that might arise because of insufficient time resolution (i.e. not saving the model output often enough).

- **Total Energy instead of Barotropic Energy**: Carter et al. (2008)'s paper analyzed the barotropic energy and the energy deviation from vertical average separately while the density field is present. Assuming the energy conversion between the barotropic (depth averaged) and non-depth averaged component is dominated by internal tide, the non-depth averaged energy component is small. In our case, because we only consider constant density case, the energy balance should take the non-depth averaged component into account and this will likely improve the balance of the energy for r_{23}, and probably even for r_{21}. This should provide the biggest contribution to the energy imbalance that we see for r_{23}.

- **Different Choices for Eddy Coefficients**: The horizontal and the vertical eddy coefficients were not chosen carefully to target this analytical model. For example, the vertical eddy coefficient that we used for Kyuquot Sound is a general accepted coefficient in barotropic mode ($K_m = 0.02$ m^2/s), the bottom

frictional coefficient is 0.0025, and we did not vary these coefficients throughout the runs; the horizontal eddy coefficient in r_{23} ($C = 1.0$) is a widely used number for the horizontal eddy coefficient. A more careful and thorough comparison could be done by fixing the horizontal eddy coefficient and vary the vertical eddy coefficient for more runs to compare the results.

- **Different Interpolation Methods**: As what we have discussed earlier, the vector and scalar variables are interpolated differently in FVCOM and in this thesis because they are located at different positions in triangles. If we were to do a more careful energy budget, we should follow exactly what FVCOM is evaluating each of the flux variable (both internal and external), and calculate the energy budget accordingly. Again, fortunately, this is not one of the objects of the thesis and the current energy calculation method is sufficient for our purpose.

- **Larger Time Step**: The time step we chose for the simulations were originally bounded by much smaller horizontal eddy coefficients that were not used in this study. We can potentially increase the the time step up to 0.3 s (from CFL criteria, but might not be able to get this large) so we can run more simulations within given time and resource constraints to have a better understanding of how energy is dissipated (i.e. numerical dissipation v.s. actual dissipation).

6.2 Future Work

In this thesis, we only examined the barotropic M_2 tidal circulation in Kyuquot Sound. How the circulation responses to a combination of tidal constituents in baroclinic condition (with temperature, salinity, and density fields) is to be investigated. Most importantly, if we use the simple analytical model to predict current circulation in reality for mostly navigation and aquaculture purposes, it needs to have the ability to deal with stratified flow and wind stress, and this ability is to be verified. Furthermore, we would like to see if the simple analytical model is general enough to be used in other geographically similar locations (i.e. a primary and a secondary channel share a joint non-seaside point, such as Puget Sound, Strait of Georgia and Juan de Fuca Strait). These results can be tested against either more numerical models or field observations.

It will be difficult to verify the analytical model in terms of energy balance if a large component of dissipation comes from numerical dissipation. It will give us a better understanding to the limitations of the simple analytical model if we could identify where the numerical dissipation occurs and quantify how much it is in the numerical results of FVCOM. However, the numerical dissipation could affect the results differently once we introduce stratifications in the model.

Appendix A

Appendices and Additional Information

A.1 Least-Square Linear Approximation for $\frac{\partial u}{\partial x}$:

The velocities from the model results were only given at centres of every element's. FVCOM uses the least square linear approximation for velocities distribution within an element. Assume the velocity in the middle cell is $u_0(x_0, y_0)$, and velocities at three adjacent cells are $u_1(x_1, y_1)$, $u_2(x_2, y_2)$, and $u_3(x_3, y_3)$. From FVCOM manual, it uses least square linear approximation. We assume solution has the form:

$$u(x, y) = u_0 + \frac{\partial u}{\partial x}(x - x_0) + \frac{\partial u}{\partial y}(y - y_0) \tag{A.1}$$

where we need to estimate the unknowns:

$$a = \frac{\partial u}{\partial x} \tag{A.2}$$

$$b = \frac{\partial u}{\partial y} \tag{A.3}$$

and $u_0(x_0, y_0)$ is actually known from FVCOM results. substituting for the values in the 3 neighbouring elements, we get

$$u_1 = u_0 + a(x_1 - x_0) + b(y_1 - y_0) \tag{A.4}$$
$$u_2 = u_0 + a(x_2 - x_0) + b(y_2 - y_0) \tag{A.5}$$
$$u_3 = u_0 + a(x_3 - x_0) + b(y_3 - y_0) \tag{A.6}$$

In matrix form:

$$\begin{bmatrix} x_1 - x_0 & y_1 - y_0 \\ x_2 - x_0 & y_2 - y_0 \\ x_3 - x_0 & y_3 - y_0 0 \end{bmatrix} \begin{pmatrix} a & b \end{pmatrix} = \begin{bmatrix} u_1 - u_0 \\ u_2 - u_0 \\ u_3 - u_0 \end{bmatrix} \tag{A.7}$$

Simplify $x_1 - x_0$ to x_{10} etc., and set $z_1 = u_1 - u_0$:

$$\begin{bmatrix} x_{10} & y_{10} \\ x_{20} & y_{20} \\ x_{30} & y_{30} \end{bmatrix} \begin{pmatrix} a & b \end{pmatrix} = \begin{bmatrix} z_1 \\ z_2 \\ z_3 \end{bmatrix} \tag{A.8}$$

This is an overdetermined system that we can solve via least squares. Set

$$J = (z_1 - ax_{10} - by_{10})^2 + (z_2 - ax_{20} - by_{20})^2 + (z_3 - ax_{30} - by_{30})^2 \tag{A.9}$$

Then the least squares solution is given by setting $\frac{\partial J}{\partial a} = \frac{\partial J}{\partial b} = 0$:

$$\frac{\partial J}{\partial a} = -2x_{10}(z_1 - ax_{10} - by_{10}) - 2x_{20}(z_2 - ax_{20} - by_{20}) - 2x_{30}(z_3 - ax_{30} - by_{30}) = 0 \tag{A.10}$$

$$\frac{\partial J}{\partial b} = -2y_{10}(z_1 - ax_{10} - by_{10}) - 2y_{20}(z_2 - ax_{20} - by_{20}) - 2y_{30}(z_3 - ax_{30} - by_{30}) = 0 \tag{A.11}$$

and:

$$a(x_{10}^2 + x_{20}^2 + x_{30}^2) + b(x_{10}y_{10} + x_{20}y_{20} + x_{30}y_{30}) = x_{10}z_1 + x_{20}z_2 + x_{30}z_3 \tag{A.12}$$

$$a(x_{10}y_{10} + x_{20}y_{20} + x_{30}y_{30}) + b(y_{10}^2 + y_{20}^2 + y_{30}^2) = y_{10}z_1 + y_{20}z_2 + y_{30}z_3 \qquad \text{(A.13)}$$

In Matrix form:

$$\begin{bmatrix} x_{10}^2 + x_{20}^2 + x_{30}^2 & x_{10}y_{10} + x_{20}y_{20} + x_{30}y_{30} \\ x_{10}y_{10} + x_{20}y_{20} + x_{30}y_{30} & y_{10}^2 + y_{20}^2 + y_{30}^2 \end{bmatrix} \begin{bmatrix} a \\ b \end{bmatrix} = \begin{bmatrix} x_{10}z_1 + x_{20}z_2 + x_{30}z_3 \\ y_{10}z_1 + y_{20}z_2 + y_{30}z_3 \end{bmatrix} \qquad \text{(A.14)}$$

Therefore:

$$\begin{bmatrix} \frac{\partial u_0}{\partial x} \\ \frac{\partial u_0}{\partial y} \end{bmatrix} = \begin{bmatrix} x_{10}^2 + x_{20}^2 + x_{30}^2 & x_{10}y_{10} + x_{20}y_{20} + x_{30}y_{30} \\ x_{10}y_{10} + x_{20}y_{20} + x_{30}y_{30} & y_{10}^2 + y_{20}^2 + y_{30}^2 \end{bmatrix}^{-1} \begin{bmatrix} x_{10}z_1 + x_{20}z_2 + x_{30}z_3 \\ y_{10}z_1 + y_{20}z_2 + y_{30}z_3 \end{bmatrix} \qquad \text{(A.15)}$$

A.2 Discretely Evaluating Pressure Gradient $\frac{\partial \eta}{\partial x}$:

Here we apply the divergence theorem: Three nodes define every element in FVCOM and let us name them as $j = N1, N2, N3$, counting clockwise. Sea surface elevations (η) are given at every nodes. Denote them at the three nodes by $\eta(N1)$, $\eta(N2)$ and $\eta(N3)$. The surface integral of the pressure gradient can be converted to a line integration using the divergence theorem. Denote the three nodes' coordinates by (x_1, y_1), (x_2, y_2), and (x_3, y_3). Discretely, we can express the integration as (FVCOM manual page 26, 2011 version):

$$\begin{aligned} \int_x \int_y \frac{\partial \eta}{\partial x} dy dx &= \frac{1}{2}\left(\eta(N1) + \eta(N2)\right)(y_1 - y_2) \\ &+ \frac{1}{2}\left(\eta(N2) + \eta(N3)\right)(y_2 - y_3) \\ &+ \frac{1}{2}\left(\eta(N3) + \eta(N1)\right)(y_3 - y_1) \qquad \text{(A.16)} \\ \int_x \int_y \frac{\partial \eta}{\partial y} dy dx &= \frac{1}{2}\left(\eta(N1) + \eta(N2)\right)(x_2 - x_1) \\ &+ \frac{1}{2}\left(\eta(N2) + \eta(N3)\right)(x_3 - x_2) \\ &+ \frac{1}{2}\left(\eta(N3) + \eta(N1)\right)(x_1 - x_3) \qquad \text{(A.17)} \end{aligned}$$

Note: the grid input file lists all elements in counte- clockwise order. But in file: getdim.F, it reverses the order. The order that FVCOM uses to compute flux is actually clockwise.

Appendix B

Bibliography

Bibliography

Beach, W. P. and M. W. Stacey, 2005: Review of the Partition of Tidal Energy in Five Canadian Fjords. *Energy*, **(1961)**, 731–746, doi:10.2112/002-NIS.1.

Blumberg, A. and G. Mellor, 1987: A Description of a Three-dimensional Coastal Ocean Circulation Model. *Three Dimensional Coastal Ocean Models*, N. S. Heaps, Ed., Washington, DC, 1–16.

Bretschneider, D., G. Cannon, J. Holbrook, and D. Pashinski, 1985: Variability of Subtidal Current Structure in a Fjord Estuary: Puget Sound, Washington. *Journal of Geophysical Research*, **90 (5)**, 1949–1958.

Carter, G., et al., 2008: Energetics of M2 Barotropic-toBaroclinic Tidal Conversion at the Hawaiian Islands. *Journal of Physical Oceanography*, **38 (October)**, 2205–2222.

Cartwright, D., J. Huthnance, R. Spencer, and J. Vassie, 1980: On the St Kilda shelf tidal regime. *Deep Sea Research Part A. Oceanographic Research Papers*, **27 (1)**, 61–70, doi:10.1016/0198-0149(80)90072-2, URL `http://linkinghub.elsevier.com/retrieve/pii/0198014980900722`.

Chen, C., R. Beardsley, and G. Cowles, 2006: An Unstructured Grid , Finite-Volume Coastal Ocean Model FVCOM User Manual. Tech. Rep. JULY, 315 pp.

Chen, C., H. Huang, R. Beardsley, H. Liu, Q. Xu, and G. Cowles, 2007: A finite volume numerical approach for coastal ocean circulation studies: Comparisons with finite difference models. *Journal of Geophysical Research*, **112 (C3)**, C03 018, doi:10.1029/2006JC003485, URL `http://www.agu.org/pubs/crossref/2007/2006JC003485.shtml`.

Chen, C., H. Liu, and R. Beardsley, 2003: An Unstructured Grid, Finite-Volume, Three-Dimensional, Primitive Equations Ocean Model: Application to Coastal

Ocean and Estuaries. *Journal of Atmospheric and Oceanic Technology*, **20**, 159–186.

Chen, C., et al., 2011: Tidal dynamics in the Gulf of Maine and New England Shelf: An application of FVCOM. *Journal of Geophysical Research*, **116 (C12)**, C12 010, doi:10.1029/2011JC007054, URL `http://doi.wiley.com/10.1029/2011JC007054`.

Courant, R., K. Friedrichs, and H. Lewy, 1967: On the Partial Difference Equations of Mathematical Physics. *IBM Journal of Research and Development*, **11(2) (March)**, 215–234.

de Young, B. and S. Pond, 1987: The internal tide and resonance in Indian Arm, British Columbia. *Journal of Geophysical Research*, **92 (C5)**, 5191, doi:10.1029/JC092iC05p05191, URL `http://www.agu.org/pubs/crossref/1987/JC092iC05p05191.shtml`.

Ferziger, J. H. and M. Peric, 2002: *Computational Methods for Fluid Dynamics*. 3d ed., Springer.

Foreman, M., 1977: Manual for tidal heights analysis and prediction. *Pacific Marine Science Report 77-10*, Institute of Ocean Sciences, Patricia Bay, Sidney, BC, 97pp.

Foreman, M., 1978: Manual for tidal currents analysis and prediction. *Pacific Marine Science Report 78-6*, Institute of Ocean Sciences, Patricia Bay, Sidney, BC, 57pp.

Foreman, M., W. Crawford, J. Cherniawsky, R. Henry, and M. Tarbotton, 2000: A high-resolution assimilating Tidal Model for the northeast Pacific Ocean. *Journal of Geophysical Research*, **105**, 629–651.

Foreman, M. G. G., R. A. Walters, R. F. Henry, and C. P. Keller, 1995: A tidal model for eastern and the southern Strait of Georgia. *Journal of Geophysical Research*, **100 (C1)**, 721–740.

Freeland, H. and D. Farmer, 1980: Circulation and Energetics of a Deep, Strongly Stratified Inlet. *Can. J. Fish. Aquat. Sci.*, **37**, 1398–1410.

Garrett, C., 1975: Tides in gulfs. *Deep-Sea Research*, **22 (June 1974)**, 23–35.

Gill, A. E., 1982: *Atmosphere-Ocean Dynamics*. Academic Press, Inc., New York, 662 pp.

Godin, G., 1972: *The Analysis of Tides*. University of Toronto, Toronto, 264pp pp.

Henry, R. and R. Walter, 1993: Geometrically based, automatic generator for irregular triangular networks.pdf. *Communication in Numerical Methods in Engineering*, **9**, 555–566.

Hunt, J., 1964: Tidal Oscillations in Estuaries. *Geophysical Journal of the Royal Astronomical Society*, **8 (4)**, 440–455.

Irishab, J., W. Munk, and F. Snodgrassab, 1971: M 2 amphidrome in the northeast pacific. *Geophysical Fluid Dynamics*, **2 (1)**, 355–360, doi: 10.1080/03091927108236069.

Kelly, S. M., J. D. Nash, and E. Kunze, 2010: Internal-tide energy over topography. *Journal of Geophysical Research*, **115 (C6)**, C06 014, doi:10.1029/2009JC005618, URL `http://doi.wiley.com/10.1029/2009JC005618`.

Klymak, J. M. and M. C. Gregg, 2004: Tidally Generated Turbulence over the Knight Inlet Sill. *Journal of Physical Oceanography*, **34**, 1135–1151.

Marsaleix, P., F. Auclair, J. W. Floor, M. J. Herrmann, C. Estournel, I. Pairaud, and C. Ulses, 2008: Energy conservation issues in sigma-coordinate free-surface ocean models. *Ocean Modelling*, **20 (1)**, 61–89, doi:10.1016/j.ocemod.2007.07.005, URL `http://linkinghub.elsevier.com/retrieve/pii/S1463500307000984`.

Masson, D. and I. Fine, 2012: Modeling seasonal to interannual ocean variability of coastal British Columbia. *Journal of Geophysical Research*, **117 (C10)**, 1–14, doi:10.1029/2012JC008151, URL `http://www.agu.org/pubs/crossref/2012/2012JC008151.shtml`.

Mellor, G. and A. Blumberg, 1985: Modeling Vertical and Horizontal Diffusivities with the Sigma Coordinate System. *Monthly Weather Review*, **113**, 1379–1383.

Mellor, G. L., 2004: Users Guide for a Three-dimensional, Primitive Equation, Numerical Ocean Model. Tech. Rep. June, 37 pp.

Munk, W., 1998: Once again: once again - tidal friction. *Prog. Oceanog.*, **40**, 7–35.

Pawlowicz, R., B. Beardsley, and S. Lentz, 2002: Classical tidal harmonic analysis including error estimates in MATLAB using T_TIDE. *Computers & Geosciences*, **28 (8)**, 929–937, doi:10.1016/S0098-3004(02)00013-4, URL `http://linkinghub.elsevier.com/retrieve/pii/S0098300402000134`.

Stacey, M. W., 1984: The Interaction of Tides with the Sill of a Tidally Energetic Inlet. *J. Phys. Oceanogr.*, **14 (1105-1107)**.

Stacey, M. W., 1985: Some Aspects of the Internal Tide in Knight Inlet, British Columbia. *Journal of Physical Oceanography*, **15 (12)**, 1652–1661.

Sverdrup, H., 1942: *The Oceans Their Physics, Chemistry, and General Biology*. c1942 ed., Prentice-Hall, New York, 1087 pp.

Thomson, R. E., 1981: *Oceanography of the British Columbia Coast*. 291 pp.

Tinis, S. W. and S. Pond, 2001: Tidal Energy Dissipation at the Sill of Sechelt Inlet , British Columbia. *Journal of Physical Oceanography*, **31 (December)**, 3365–3373.

Zhong, L. and M. Li, 2006: Tidal energy fluxes and dissipation in the Chesapeake Bay. *Continental Shelf Research*, **26 (6)**, 752–770, doi:10.1016/j.csr.2006.02.006, URL `http://linkinghub.elsevier.com/retrieve/pii/S0278434306000410`.